How Moist and Dry Intrusions Control the Local Hydrologic Cycle in Present and Future Climates

Samuel Smith[1]*, Paul W. Staten[1], Jian Lu[2]

[1]Indiana University, Bloomington, IN [2]Pacific Northwest National Laboratory, Richland, WA

*Contact information: 1001 E. 10th St., Bloomington, IN 47408; samjsmit@iu.edu

1 **Abstract**

2   Models disagree on how much the hydrologic cycle could intensify under climate

3 change. These changes are expected to scale with the Clausius-Clapeyron relation but may

4 locally diverge due in part to the uncertain response of the general circulation, causing the

5 hydrologic cycle to inherit this uncertainty. To identify how the circulation contributes, we link

6 circulation changes to changes in the higher moments of the hydrologic cycle using the novel

7 dynamical framework of the local hydrologic cycle, the portion of the hydrologic cycle driven by

8 moist or dry intrusions. We expand this dynamical framework, developing a closed budget

9 which diagnoses thermodynamic, advective, and overturning contributions to future hydrologic

10 cycle changes. In analyzing these changes for the Community Earth System Model Large

11 Ensemble, we show that overturning is the main dynamic contributor to the tropical and

12 subtropical annual response, consistent with a weakening of this circulation. In the extratropics,

13 we show that advective contributions, likely from storm track changes, dominate the response.

14 We achieve a cleaner separation between dynamic and thermodynamic contributions through

15 a semi-empirical scaling, which reveals the robustness of the Clausius-Clapeyron scaling for the

16 local hydrologic cycle. This scaling also demonstrates the slowing of the local hydrologic cycle

17 and how changing subtropical dynamics asymmetrically impact wave breaking and suppress

18 meridional moisture transport. We conclude that dynamic changes in the subtropics are

19 predominantly responsible for the annual, dynamic response in the extratropics and thus a

20 significant contributor to uncertainty in future projections.

1. Introduction

Climate change will intensify the hydrologic cycle, both in the mean and the extremes (Trenberth 1999; Allen and Ingram 2002; Held and Soden 2006; O'Gorman and Schneider 2009; O'Gorman 2015; Chen et al. 2019). While this intensification will not be spatially uniform (Neelin et al. 2013; Polade et al. 2017; Lu et al. 2018; Song et al. 2018; Feng et al. 2019), confidence in this intensification stems from global energy constraints (Trenberth 1999; Held and Soden 2006) and basic thermodynamic principles (Lorenz and DeWeaver 2007; Stephens and Hu 2010). Regionally, the magnitude of hydrologic cycle changes is less certain, despite clear thermodynamic signals (O'Gorman 2015; Pfahl et al. 2017). This uncertainty is largely due to uncertainty in atmospheric circulation changes, often termed the "dynamic" response (Lu et al. 2014; O'Gorman 2015; Pfahl et al. 2017; Tandon et al. 2018; Weller et al. 2019), although other drivers of regional climate such as land-sea contrast may contribute (Byrne and O'Gorman 2015). Work to reduce uncertainty in regional changes has concentrated on isolating the dynamic or circulation-driven component of change across the probability distribution of the hydrologic cycle (O'Gorman and Schneider 2009; Seager et al. 2010; Bony et al. supp2013; Pendergrass and Gerber 2016; Pfahl et al. 2017; Tandon et al. 2018; Weller et al. 2019; Chen et al. 2019).

Despite this recent effort, delineating between dynamically- and thermodynamically-driven changes in future projections of the hydrologic cycle remains a challenge, complicated by the non-linearity of advection in the advection-diffusion-condensation problem which controls the hydrologic cycle (Neelin et al. 2010; Lu et al. 2017). Consequently, statistical methods for decomposition which rely on the empirical correlation between precipitation

3

43   amount and vertical velocity may be invalid in some regions, particularly the subtropics (Pfahl

44   et al. 2017). Physically-based methods which scale precipitation with the moist adiabatic lapse

45   rate require assumptions of large-scale saturated ascent (Pfahl et al. 2017), and they cannot

46   discriminate between the varied processes responsible for that ascent beyond the relative

47   impacts of stability and the length scale of convergence (Tandon et al. 2018). Decompositions

48   of the Eulerian column water vapor budget can result in various non-linear or higher-order

49   terms (Seager and Henderson 2013, Byrne and O'Gorman 2015, Lu et al. 2017) which are not

50   always negligible and can be challenging to compute or interpret (Seager and Henderson 2013).

51   The heterogenous nature of the dynamic component of hydrologic cycle change

52   compounds these diagnostic challenges. This dynamic component aggregates many changes in

53   the atmospheric circulation: at the largest scales, jet streams shift (Chang et al. 2012; Shaw

54   2019; Shaw et al. 2016) and Hadley circulations widen (Kang and Lu 2012; Lu et al. 2007; Staten

55   et al. 2019); at local levels, circulations respond to increased land-sea contrast (Byrne and

56   O'Gorman 2013; Joshi et al. 2008), dwindling sea-ice (Kim et al. 2014; Romanowsky et al. 2019),

57   and modified sea surface temperatures (Huang et al. 2017). Thus, narrowing the spread in

58   future projections of regional hydrologic cycle changes requires process-level understanding

59   (Liu et al. 2020; Polade et al. 2014).

60   However, understanding these dynamic changes in isolation neglects their

61   interdependence (Pendergrass and Gerber 2016; Thackeray et al. 2018). Despite this,

62   precipitation-producing ("wet") processes and precipitation-inhibiting ("dry") processes are

63   often studied separately—a natural dichotomy given the highly skewed distribution of

64   precipitation and the enormous range of climatological precipitation characteristics. While such

4

65   wet and dry speciation has yielded substantial insight (Liu et al. 2020; al Fahad et al. 2020), it

66   may obscure the relative contributions of wet and dry processes to the net response. For

67   example, understanding future changes in rain rates requires understanding changes in both

68   ascent and descent (Pendergrass and Gerber 2016). This interdependence motivates an

69   approach which focuses on the driving circulations common to all wet and dry processes. To

70   address this goal, we develop a hybrid Eulerian-Lagrangian framework to analyze the higher

71   moments of the wet and dry ends of the hydrologic cycle in present and future climates,

72   benefitting from both a closed budget equation and a diffusive scaling relationship.

73   Central to our effort is the local hydrologic cycle (LHC), introduced by Lu et al. (2017;

74   hereafter L17). Intuitively, the LHC represents the net precipitation or evaporation driven by

75   "zonally-anomalous" moisture or dryness, which we refer to as moist or dry intrusions.

76   However, the measure of zonal asymmetry used here is not the Eulerian zonal-mean (as in, e.g.,

77   Wills et al. 2016). Rather, we measure zonal asymmetry with respect to a Lagrangian

78   background state, which is more strongly constrained to Clausius-Clapeyron (CC) scaling than its

79   Eulerian counterpart, as we will demonstrate. This approach enables an alternative perspective

80   on the role of moisture transport process in dynamically and thermodynamically modifying the

81   hydrologic cycle. We define the LHC more formally in Section 2.

82   In introducing the LHC framework, L17 primarily focus on its zonal-mean formulation

83   and its application to atmospheric rivers (AR) and precipitation extremes. Lu et al. (2018;

84   hereafter L18) confirms this robust connection between the LHC and more traditional metrics

85   of precipitation extremes (see their Figure 3) while also introducing the zonally-varying LHC,

86   which they use to examine changes in AR in the Western United States. Xue et al. (2018)

5

87   similarly utilize the LHC framework to study the Asian summer monsoon. A prominent result of

88   this previous work on the LHC is that the LHC slows in response to climate change in a manner

89   analogous to that seen for the mean hydrologic cycle (i.e., Held and Soden 2006).

90   The structure of this work is outlined as follows. In Section 2, we review the LHC

91   framework and its assumptions, extend the moist framework of L17 and L18 to encompass the

92   dry component of the LHC, and develop its closed budget equation analogous to the Eulerian

93   moisture budget (e.g., Seager et al. 2010). In Section 3, we describe the Community Earth

94   System Model (CESM) Large Ensemble (LENS) dataset utilized here, along with challenges in the

95   numerical implementation of the LHC framework. In Section 4, we present our results,

96   beginning by examining advective and overturning contributions from the LHC budget in

97   Section 4a. In Section 4b, we further probe dynamic changes using the mixing length scale,

98   hydrological cycling rate, and participation ratio, finding that the slowdown of the LHC seen in

99   L17 for the wet component extends to the dry and that changing subtropical dynamics drive an

100 asymmetric response in the mixing length between the wet and dry components. In Section 4c,

101 we examine moist intrusions which transport moisture but do not participate in the LHC, with

102 implications for AR. Our results highlight the predominant role played by the large-scale

103 circulation in determining the dynamical response, suggesting that constraining changes in the

104 spatial distribution of hydrologic cycle extremes in the extratropics must begin with

105 constraining the meridional shifts in the large-scale circulation.

106

107 **2. LHC Budget Formalism**

6

108   The LHC is founded upon displacements ("intrusions") of column-integrated water vapor

109   (CWV) from a semi-Lagrangian, zonally-symmetric background state. This background state is

110   determined by conservatively "zonalizing" the zonally meandering CWV isosurfaces.

111   Schematically, this is illustrated for the Northern Hemisphere in Figure 1. For an individual

112   contour (red line), this process can be conceptualized as determining the parallel (termed the

113   *equivalent latitude*, thick black dashed line) which divides the contour into two regions of equal

114   area, one region consisting of the poleward moist intrusions (shaded in aqua) and the other of

115   the equatorward dry intrusions (shaded in tan). Equivalently, the surface area enclosed

116   poleward of the equivalent latitude is equal to that enclosed poleward of the contour. This

117   process is accomplished numerically by sorting and rearranging a gridded CWV field, taking

118   proper steps to ensure conservation of mass. Repeating this process for every equivalent

119   latitude yields the background state.

120   It bears repeating that the background state defined here is better constrained to the

121   climate state than the zonal-mean, for reasons similar to those argued by Huang and Nakamura

122   (2016) in the context of potential vorticity. Given this background state for CWV, we can now

123   utilize it to define moist and dry intrusions and to integrate the net precipitation or evaporation

124   within the moist and dry intrusions, defining the LHC.

125   To formally derive the LHC budget, we begin with the column water vapor equation,

126   which can be derived by taking the vertical integral of the familiar moisture equation (see L17

127   or Trenberth and Guillemot 1995):

128
$$\frac{\partial m}{\partial t} = (E - P) - \nabla \cdot (m\mathbf{v}). \tag{1}$$

7

129 Here m is column water vapor (CWV), E is column evaporation rate, P is column precipitation

130 rate, and $\boldsymbol{v}$ is the vertically-integrated product of specific humidity and horizontal velocity

131 normalized by the CWV. Since the velocity is weighted by specific humidity, $\boldsymbol{v}$ can be thought of

132 as the lower-tropospheric-mean horizontal velocity. Due to data availability constraints, we

133 approximate column evaporation rate E and precipitation rate P with their surface rates. This

134 does not account for the possibility of "teleportation" of CWV where water vapor is condensed,

135 advected out of the column, and re-evaporated elsewhere, but we find these errors, in

136 conjunction with model failure to conserve water mass, to be small, as in L17.

137   To focus on moist and dry intrusions and remove the background state, we utilize the

138 local wave activity (LWA) transformation. LWA is a conservative line-integral transformation

139 given by

$$\widetilde{(\ )} = \widetilde{(\ )}^{+} - \widetilde{(\ )}^{-} = \frac{a}{\cos \phi_e} \int_{m>M,\phi>\phi_e} (\ ) \cos \phi \, d\phi - \frac{a}{\cos \phi_e} \int_{m<M,\phi<\phi_e} (\ ) \cos \phi \, d\phi, \quad (2)$$

141 where a is the radius of the earth, ϕ is latitude, ϕ_e is the equivalent latitude, and M is the

142 background state CWV. $\widetilde{(\ )}^{+}$ denotes integration over moist intrusions, and $\widetilde{(\ )}^{-}$ denotes

143 integration over dry intrusions. For further discussion of the LWA transformation, we refer the

144 reader to the literature (in particular, L17, L18 and Xue et al. 2018; but also Huang and

145 Nakamura 2016, 2017; and Nakamura and Solomon 2010, among others).

146   Applying the LWA transformation (2) to the CWV field yields the moist (A^+) and dry

147 wave activity (A^-), which measure the amplitude of moist and dry intrusions, given by

$$A = A^+ - A^- \equiv \widetilde{(m)}^+ - \widetilde{(m)}^-. \quad (3)$$

8

149   We apply (2) to the full CWV field, instead of the more common choice for wave activities of

150   the eddy field, as background state moisture still plays an important role in the generation of

151   moist intrusions, as we will show. The CWV budget equation can be similarly transformed using

152   LWA to produce the LHC budget. Changes in this budget will reveal changes which are driven by

153   the background state M, which we term the "thermodynamic" component of the budget, and

154   those which are driven by advective or overturning processes.

155   Integrating the CWV budget (1) using the definition of LWA (2) and of wave activity (3),

156   and simplifying with the Leibniz integral rule, we yield the basic LHC budget:

157
$$\frac{\partial}{\partial t}(A - M\eta) = (\widetilde{E - P}) - [\widetilde{\boldsymbol{\nabla} \cdot (m\mathbf{v})}]. \tag{4}$$

158   Here η represents the meridional extent of a moist intrusion or its mixing length, which will be

159   discussed in more detail later. While further simplification of this budget will lead to greater

160   insight, the basic budget has several important features. Most importantly,

161
$$(\widetilde{P - E}) \equiv (\widetilde{P - E})^{+} + (\widetilde{E - P})^{-} \tag{5}$$

162   represents the LHC, broken into wet and dry components (grey contours in Figure 1). This

163   definition reveals the LHC to be the net precipitation (evaporation) connected with moist (dry)

164   intrusions, from processes such as warm conveyor belts, AR, low-level jets, or blocks. Since such

165   events are frequently responsible for wet and dry extremes, the LHC agrees well with more

166   traditional measures, such as the 99%-ile of $P - E$ (L18; Xue et al. 2018).

167   Eq. (4) reveals that the LHC is balanced by the tendency of the adjusted wave activity

168    $(A - M\eta)$ and by the local moisture flux convergence (2nd term, rhs, black arrows in Figure 1).

9

169   The wave activity must be adjusted because of our choice to include the background state in

170   our definition of wave activity, even though the background state itself does not drive the LHC.

171   Importantly, the adjusted mean wave activity tendency is negligible on annual to decadal time

172   scales because surface temperatures largely determine atmospheric moisture storage. This

173   suggests that the dominant balance in (4) is between the LHC and the local moisture flux

174   convergence; we will henceforth neglect the tendency. This introduces slight errors in the moist

175   budget for the annual-mean (Supplemental Figure 1) and well-defined seasons and larger (but

176   still small) errors in the dry budget (Supplemental Figure 1) and shoulder seasons.

177   To further simplify the basic budget (4) to gain further insight into the LHC, we partition

178   m into a linear combination of the background state M and the intrusions, $m_e \equiv m - M$. We

179   further apply Leibniz rule and split the horizontal velocity $\mathbf{v}$ into zonal u and meridional v

180   components, aided by the integration of the moisture flux divergence $[\boldsymbol{\nabla} \cdot \widetilde{(m\mathbf{v})}]$ over a closed

181   domain. This yields the following budget:

$$\widetilde{(P - E)} = -M(\widetilde{\boldsymbol{\nabla} \cdot \mathbf{v}}) + m_e v - \frac{\partial}{\partial x}\left[\widetilde{(m_e u)}\right]. \tag{6}$$

183   Here we use $\frac{\partial}{\partial x} \equiv \frac{1}{a \cos \phi_e} \frac{\partial}{\partial \lambda}$ (λ being longitude) for brevity. (6) is developed more rigorously

184   from (1) in Supplemental Section 1.

185   Defining $\delta \equiv (6)_{future} - (6)_{present}$ as changes in (6) from present (1990-2005) to

186   future (2071-2080) climates, we decompose the annual-mean changes in the LHC budget:

$$\delta\widetilde{(P - E)} = -(\delta M)\overline{(\widetilde{\boldsymbol{\nabla} \cdot \mathbf{v}})} - \overline{M}\delta\left[\widetilde{(\boldsymbol{\nabla} \cdot \mathbf{v})}\right] + \delta(m_e v) - \delta\left\{\frac{\partial}{\partial x}\left[\widetilde{(m_e u)}\right]\right\}. \tag{7}$$

10

188 Here the overbar $\overline{(\ )} \equiv \frac{1}{2}\left[(\ )_{future} + (\ )_{present}\right]$ signifies the mean over both climates. In

189 deriving (7), we neglect the cross term $\delta\left\{\overline{M'(\widetilde{\boldsymbol{\nabla}\cdot\mathbf{v}})'}\right\}$ (prime terms being deviations from the

190 time mean). This term varies primarily on seasonal timescales and does not change greatly

191 between climate states (not shown). Thus, it represents a negligible fraction of the total annual

192 and monthly changes. Ignoring this cross term means our decomposition tends to overpredict

193 the magnitude of the changes mildly, but by less than 10% (see Supplemental Figure 1).

194 Neglecting this term is not essential to our method nor does it impact our conclusions.

195 As a final step, the changes in the budget given in (7) are separated into moist and dry

196 contributions, which is a unique advantage of this approach. Since moist intrusions (m_e^+) and

197 dry intrusions (m_e^-) are computed separately, we can consequently apply this decomposition to

198 moist and dry intrusions separately:

199
$$\delta(\widetilde{P-E})^+ = -(\delta M)\overline{(\widetilde{\boldsymbol{\nabla}\cdot\mathbf{v}})^+} - \overline{M}\delta\left[(\widetilde{\boldsymbol{\nabla}\cdot\mathbf{v}})^+\right] + \delta(m_e^+ v) - \delta\left\{\frac{\partial}{\partial x}\left[(\widetilde{m_e u})^+\right]\right\} \quad (8a)$$

200
$$\delta(\widetilde{E-P})^- = \underbrace{(\delta M)\overline{(\widetilde{\boldsymbol{\nabla}\cdot\mathbf{v}})^-}}_{\text{thermodynamic}} + \underbrace{\overline{M}\delta\left[(\widetilde{\boldsymbol{\nabla}\cdot\mathbf{v}})^-\right]}_{\text{overturning}} - \underbrace{\delta(m_e^- v)}_{\substack{\text{meridional}\\\text{advection}}} + \underbrace{\delta\left\{\frac{\partial}{\partial x}\left[(\widetilde{m_e u})^-\right]\right\}}_{\substack{\text{zonal LWA flux}\\\text{convergence}}}. \quad (8b)$$

201 Each of the four terms on the rhs of (8) give some insight into what processes are physically

202 responsible for modulating the LHC in a changing climate (see Supplemental Figure 2). The first

203 term, $(\delta M)\overline{(\widetilde{\boldsymbol{\nabla}\cdot\mathbf{v}})}$, represents the contributions from the increasingly moist background state

204 M, weighted by the mean convergence (divergence); it therefore captures the dominant

205 thermodynamic influences in the decomposition. The second term, $\overline{M}\delta\left[(\widetilde{\boldsymbol{\nabla}\cdot\mathbf{v}})\right]$, quantifies

206 contributions from changes in the low-level convergence of background moisture and is

11

207   intimately linked to changes driven by a weakening overturning circulation (Held and Soden

208   2006, Vecchi and Soden 2007) and increasing static stability (Kang and Lu 2012, He and Soden

209   2017). The third term, $\delta(m_e v)$, corresponds to changes driven by meridional advection of

210   moist or dry intrusions. It captures the primary contributions of phenomena which transport

211   large amounts of moisture or dryness meridionally, such as AR and cyclones (tropical or

212   extratropical) in the moist case, or anticyclones in the dry case. The final dynamic term,

213     $\delta\left\{\frac{\partial}{\partial x}\left[\widetilde{(m_e u)}\right]\right\}$, is the zonal local wave activity (LWA) flux convergence and consists of changes

214   in zonal variations in the zonal transport of moist or dry intrusions, which are prominent in jet-

215   entrance, jet-exit, and coastal regions. By construction, the zonal LWA flux convergence term

216   does not contribute to changes in the zonal-mean LHC (see L17). Given the predominantly

217   rotational nature of the low-level extratropical flow, the zonal LWA flux convergence term

218   largely offsets the meridional advection term. In designating contributions as "advective"

219   (meridional advection and zonal LWA flux convergence terms) or "overturning", we note that

220   these are not orthogonal like the result of a Helmholtz decomposition, rather they reflect the

221   dominant circulation regimes responsible for the resulting precipitation or evaporation.

222   Because the background state M is so fundamental to understanding the LHC and it

223   drives the thermodynamic contributions, we argue here why it is expected to follow CC scaling

224   under climate change. To begin, we define CWV saturation fraction $\sigma \equiv \frac{M}{M_s}$, where M_s is the

225   saturation background state CWV, the temperature-controlled upper bound on the background

226   state CWV. To first order, we assume saturation CWV M_s responds to column temperature

227   changes in the same fashion as saturation specific humidity (e.g., Lorenz and DeWeaver 2007).

12

228   Denoting mass-weighted, vertically-averaged ($\langle \; \cdot \; \rangle$), CWV contour-following ($\widetilde{(\; \cdot \;)}$)

229   temperature as $\langle \widetilde{T} \rangle$, this implies $M_s \sim M_0 \exp\left(-L_v\left(R_{WV}\langle\widetilde{T}\rangle\right)^{-1}\right)$, where M_0 is an unimportant

230   baseline constant for M_s. Thus, we expect the background state to behave as

$$M \sim \sigma M_0 \exp\left(-L_v\left(R_{WV}\langle\widetilde{T}\rangle\right)^{-1}\right). \tag{9}$$

231

232   We now divide future state (subscript 2) by present state (subscript 1) and assume

233   column saturation fraction does not change greatly between climate states (similar to the

234   assumption of constant relative humidity, e.g., Held and Soden 2000). This assumption works

235   reasonably well in most regions, which we will validate in Section 4b. We also replace the

236   vertically-averaged temperature with the surface temperature since it is mass-weighted. This

237   gives

$$\frac{M_2}{M_1} \sim \exp\left(\alpha\Delta\widetilde{T}_s\right), \tag{10}$$

238

239   where $\alpha \approx L_v R_{WV}^{-1}(\widetilde{T}_s)^{-2}$, which should be roughly constant between climate states. Therefore,

240   we expect changes in background zonal-mean CWV to scale in accordance with CC relation as

241    $\Delta(\ln M) \sim \alpha\Delta\widetilde{T}_s$ (c.f., Lorenz and DeWeaver 2007; O'Gorman and Muller 2010).

242

243   **3. Data & Methods**

244   To analyze the LHC response to climate change, we utilize archived data from the

245   Community Earth System Model, version 1 (CESM) Large Ensemble (LENS). Briefly, CESM LENS is

246   an approximately $1.25° \times 1°$ coupled Earth system model simulation comprised of 40 members

13

247   started with varying initial conditions. A detailed description of the CESM LENS experiments is

248   outlined in Kay et al. (2014). Six hourly data including precipitation, latent heat flux, surface

249   temperature, specific humidity, velocity, surface pressure and surface geopotential height were

250   downloaded from the National Center for Atmospheric Research. Having 40 ensemble

251   members increases the ability to reduce internal climate variability, allowing for clearer

252   identification of the forced response and of uncertainty related to internal variability. In this

253   case, the response is forced by RCP 8.5, the high emissions pathway which would result in a

254   global radiative forcing of 8.5 $W\ m^{-2}$ by 2100.

255   From the downloaded data, we compute CWV and CWV-weighted velocity according to

256   L17 (see their equation 2), and then apply the wave activity transformation (2) at each gridpoint

257   for the Eulerian-equivalent terms in (8). Lagrangian quantities such as m_e cannot be properly

258   handled by the numerical routine, thus we use the equivalence $\frac{\partial}{\partial x}\left[\widetilde{(m_e u)}\right] \equiv \frac{\partial}{\partial x}\left[\widetilde{(mu)}\right] -$

259     $M\frac{\partial}{\partial x}\left[\widetilde{(u)}\right]$ to diagnose the zonal convergence term.

260   The result of the wave activity transformation is that data appear at their equivalent

261   latitude rather than their actual latitude. Since CWV increases moving equatorward, the

262   equivalent latitude for moist wave activity is equatorward of its actual latitude and vice versa

263   for the dry wave activity. This produces some artefacts, with a "squeezing" of the moist LHC at

264   the equator and of the dry LHC at the poles. However, we do not correct for this because there

265   is not a one-to-one mapping between the actual latitude of precipitation and its equivalent

266   latitude. Nevertheless, as argued by L17 (see their Figure 3), the vast majority of intrusions are

267   within 5° of their equivalent latitude and the resulting center of precipitation is typically within

14

268 10°. The displacement between the precipitation center and the equivalent latitude is greatest

269 in the subtropics, where the moisture transport function dominates the condensation function.

270   Further artefacts are introduced in the dry LHC budget by orography, which appears as a

271 dry "island" with an equivalent latitude near the poles. Since these artefacts are local to

272 orography, we mask all parts of the LHC (moist and dry) whenever the surface exceeds 800m in

273 height, and we mask poleward of the Himalayan Plateau for the dry LHC. While some proposals

274 exist to correct for these artefacts, they are prohibitively computationally expensive and thus

275 are left for implementation in future work.

276

277 **4.   Results and Discussion**

278 *a.   Processes behind hydrologic cycle change*

279   The present-day (1990-2005) climatology of the wet LHC (Figure 2a) in CESM LENS

280 highlights regions of heavy precipitation, particularly emphasizing regions upstream of large

281 moisture transport (black arrows), storm tracks, and the intertropical convergence zone (ITCZ).

282 The good agreement between the low-level circulation and the spatial distribution of the LHC

283 gives confidence that the non-locality discussed in Section 3 is generally small. Examining

284 RCP8.5 fractional changes (2071-2080 minus 1990-2005, divided by 1990-2005) in the wet LHC

285 (Figure 2b), we see a spatial pattern analogous to the wet-gets-wetter, dry-gets-drier pattern

286 previously found for hydrologic cycle change (e.g., Held and Soden 2006). Fractional changes

287 show decreases in the subtropics, where the present-day is near zero, modest increases in the

288 extratropics (with a notable local maximum in the North Atlantic, to be discussed in more detail

15

289   later), where the LHC is largest in the present-day, and only faint increases in the deep tropics.

290   The latter result should be understood primarily as a consequence of the LWA transformation

291   which leads to a "squeezing" of Eulerian features near the equator and a small discontinuity at

292   the equator itself.

293   There are two important results seen in the fractional change of the wet LHC. First,

294   while the wet LHC tends to increase where it is wet and decrease where it is dry, the fractional

295   changes shown here stray from the scaling of Held and Soden (2006), which predicts fractional

296   changes which mirror surface temperature changes. The breakdown of this scaling for the LHC

297   is consistent with the breakdown seen for the Eulerian zonally-anomalous hydrologic cycle,

298   where stationary eddy contributions generally show a spatial pattern of expansion rather than

299   thermodynamic intensification (Wills et al. 2016). The other important result seen in these

300   changes is the relatively good agreement between ensemble members (indicated by lack of

301   stippling in Figure 2b, which measures ensemble *disagreement*). The ensemble disagreement in

302   future wet LHC changes is primarily seen on the edges of subtropical dry zones, suggesting that

303   the disagreement may primarily be on the extent of subtropical expansion.

304   As might be anticipated, the climatology of the dry LHC (Figure 2c) stands out in the

305   subtropics and over major ocean evaporation basins, with subtropical stationary circulations

306   (black arrows) strongly influencing the spatial distribution. It is small over the land surface,

307   likely due to soil moisture limiting evaporation. RCP8.5 fractional changes in the dry LHC (Figure

308   2d) reveal the poleward expansion of the subtropical dry zones alongside a robust increase in

309   most regions for evaporation connected with dry intrusions, with some modest weakening in

310   the equatorial Pacific and over some land regions. Despite robust increases in the dry LHC,

16

311   many of these regions also exhibit increases in the wet LHC, highlighting the compensating

312   effects of hydrologic cycle intensification. These changes in the dry LHC further suggest that a

313   simple thermodynamic scaling such as the dry-gets-drier paradigm does not adequately explain

314   LHC changes. They also foreshadow the consistent storyline of this work that the subtropical

315   expansion and precipitation decline has profound impacts on the wet and dry ends of the LHC.

316   We now diagnose the components of the LHC and its changes using (8). The spatial

317   pattern of the present-day wet LHC is broadly set by the large-scale convergence of background

318   moisture ($M(\widetilde{\boldsymbol{\nabla} \cdot \mathbf{v}})^{+}$; Figure 3a), which is strongest near the ITCZ but also contributes on the

319   equatorward flank of storm track regions, reflecting the influence of overturning circulations.

320   Meridional advection of moist intrusions ($m_e^{+} v$; Figure 3c) tends to have local maxima in storm

321   track regions, reflecting the importance of moisture transport for these regions. As expected, a

322   portion of this meridional advection is offset by the zonal moist local wave activity (LWA) flux

323   convergence ($\frac{\partial}{\partial x}\left[(\widetilde{m_e u})^{+}\right]$; Figure 3e).

324   As with the moist case, the spatial structure of the present-day dry LHC is set by the

325   spatial pattern of divergence of background moisture ($M(\widetilde{\boldsymbol{\nabla} \cdot \mathbf{v}})^{-}$; Figure 3b), which is

326   connected with large-scale overturning. It is largest in the subtropics, with negative values

327   (green shading) likely being artefacts of orography. Meridional advection of dry anomalies

328   ($m_e^{-} v$; Figure 3d) also exhibit local maxima in the subtropics and equatorward of storm tracks in

329   regions of anticyclonic wave breaking. As before, the zonal divergence of dry LWA

330   ($\delta\left\{\frac{\partial}{\partial x}\left[(\widetilde{m_e u})^{-}\right]\right\}$; Figure 3f) offsets some of the meridional advection.

331   The results of this decomposition into overturning and advective components shows

332   that our budget-based decomposition can identify contributions to the LHC based on their

333   associated circulation regime. While it is not unique in this capacity (e.g., Seager and Henderson

334   2013, Chen et al. 2019), our decomposition is rooted in the processes which produce or

335   suppress precipitation and thus provides a new perspective to link changes in the circulation to

336   the hydrologic cycle. To begin, we apply (8), normalized by the present-day LHC, to yield the

337   RCP8.5 fractional changes. The "thermodynamic" contributions, $(\delta M)(\overline{\widetilde{\nabla \cdot \mathbf{v}}})$, behave similarly

338   between wet and dry budgets and agree with CC scaling in most regions (Figure 4a,b). The

339   addition of the convergence weighting $((\overline{\widetilde{\nabla \cdot \mathbf{v}}}))$ does lead to some zonal variations from CC

340   scaling, particularly for the moist case. The dry thermodynamic response is largely positive,

341   even with increasing background CWV, partially because an increase in water vapor holding

342   capacity increases both vapor pressure deficit and the local slope of the CC-relation,

343   strengthening evaporation (Scheff and Frierson 2014).

344   Examining the contributors beyond the background state, we see that overturning

345   contributions to the wet LHC $(\overline{M}\delta[(\widetilde{\nabla \cdot \mathbf{v}})^+]$; Figure 4c) weaken it; possibly due to the

346   weakening in the overturning circulation (Vecchi and Soden 2007) or the increase in dry static

347   stability (Kang and Lu 2012; He and Soden 2017) suppressing large-scale convection.

348   Overturning contributions to the dry LHC $(\overline{M}\delta[(\widetilde{\nabla \cdot \mathbf{v}})^-]$; Figure 4d) dominate the structure of

349   changing dry intrusions, with prominent suppression of dry intrusions (green shading) in most

350   regions, particularly the equatorial Pacific. Despite the importance of weakening divergence for

351   enhancing the dry LHC, it remains unclear whether this weakening is due to the increase in the

18

352   effective dry stability and subsequent weakening of downward motion in a warming climate

353   (Tamarin-Brodsky and Hadas 2019), the weakening of tropical large-scale overturning and its

354   associated subsidence (Vecchi and Soden 2007), the weakening of radiatively-driven subsidence

355   by the longwave effects of increased greenhouse gases (Bony et al. 2013), or some combination

356   of the above. Amidst this suppression, overturning contributions in the North Atlantic region

357   act to enhance the dry LHC. One possible interpretation here is an expansion of subtropical dry

358   zones and the poleward shift of storm tracks, both of which may allow for deeper propagation

359   of dry waves into the midlatitudes.

360   Turning to contributions from advective circulations, meridional moist advection

361   ($\delta(m_e^+ v)$; Figure 4e) dominates dynamic wet LHC changes in the mid-latitudes, particularly in

362   storm track regions, as expected. Close comparison of the changes with present-day

363   contributions (Figure 3c) reveals a modest poleward shift and intensification. This poleward

364   shift is consistent with previous work (Chang et al. 2012, Tamarin-Brodsky and Kaspi 2017),

365   although some studies, even those specifically examining CESM LENS, do not see dynamic

366   intensification (Wang et al. 2017; Peings et al. 2017; Yettella and Kay 2017). In part, this

367   difference could be due to the nature of the LHC compared to Eulerian metrics, as the former

368   emphasizes the area of an intrusion and the latter emphasizes its temporal variance (Chang et

369   al. 2012). Supporting this interpretation, Lagrangian compositing of extratropical cyclones in

370   CESM LENS has shown that individual storms produce more precipitation, while their frequency

371   and lifetime get reduced (Yettella and Kay 2017). This difference also foreshadows the residual

372   thermodynamic influences in the advective term, which will be further discussed in section 4b.

373   Changes in meridional dry advection ($\delta(m_e^- v)$; Figure 4f) are generally a weak but

374   positive (drying) contributor to the dry LHC. The relative zonal homogeneity here suggests it

375   may reflect the thermodynamic contributions of an increasing background moisture gradient.

376   An important exception here is near North Africa and the Mediterranean, where there is a local

377   maximum in dry advection contributions that is largely offset by other changes.

378   The zonal moist LWA flux convergence ($\delta\left\{\frac{\partial}{\partial x}\left[(\widetilde{m_e u})^+\right]\right\}$; Figure 4g) is responsible for

379   much of the heterogeneity of the wet LHC response. This term contributes positively (wetting)

380   on the western boundary of continental landmasses, particularly over the western coast of the

381   United States, both in the annual mean (Figure 3g) and in DJF (not shown here). Because zonal

382   LWA flux convergence can be generated by landfalling AR, increases of AR along the North

383   American Pacific coast (Gao et al. 2015; Hagos et al. 2016; L18) may explain the increases seen

384   here. Orography generally enhances this flux convergence on its windward (western, c.f. Figure

385   2a) side and suppresses it on the leeward (eastern) side, although some influence of orographic

386   artefacts (as discussed in Section 3) cannot be ruled out. There is a local maximum in

387   contributions from the flux convergence in the jet exit region of the North Atlantic. This could

388   be attributable to the cooler sea surface temperatures (SST) resulting from the North Atlantic

389   warming hole (Menary and Wood 2018), which could trigger condensation for relatively

390   warmer parcels zonally advected into the region.

391   The dry zonal LWA flux divergence ($\delta\left\{\frac{\partial}{\partial x}\left[(\widetilde{m_e u})^-\right]\right\}$; Figure 4h) is a crucial avenue for

392   subtropical expansion of the dry LHC, particularly in the North Atlantic and South Pacific where

393   subtropical anticyclones strengthen (He et al. 2017). Consistent with Scheff and Frierson (2012),

20

394   who suggest that uncertainty in extratropical precipitation change predominantly results from

395   subtropical expansion, we find this flux divergence term to be more uncertain (i.e., more

396   stippling) than the other LHC contributors. Intriguingly, the zonal divergence appears to play a

397   larger role than the meridional advection in determining the spatial structure of dry LHC

398   changes. This suggests that an increase in the magnitude of dry intrusions (m_e^-, which appears

399   in both advective terms) is not sufficient to explain the advective changes. This is significant

400   because m_e is partly thermodynamic, as we now explain.

401

402   *b. Isolating Dynamic Changes*

403   Because advective terms are influenced by a steepening moisture gradient, they do not

404   represent purely "dynamic" contributions to the LHC. While these budget terms do not

405   explicitly contain the background state M, a simple diffusive picture (e.g., Vallis 2006, Caballero

406   and Hanley 2012) of a moist or dry intrusion suggests that its magnitude ($m_e \sim \frac{\partial M}{\partial y}\eta$) depends

407   on its mixing length (η) and the gradient ($\frac{\partial M}{\partial y}$) it is mixed across. Changes in this gradient are

408   essentially a thermodynamic response given the exponential response of the background state

409   (i.e., CC scaling, also see Caballero and Hanley 2012).

410   To demonstrate that the background gradient obeys CC scaling like the background

411   state, we derive a scaling for it by taking the meridional gradient of (9) and taking the ratio

412   between future and present climate states, as before. We also neglect terms which do not

413   contribute in the first order. The result, derived more rigorously in Supplemental Section 2, is

21

$$\frac{\frac{\partial M_2}{\partial y}}{\frac{\partial M_1}{\partial y}} \sim \frac{\frac{\partial \widetilde{T}_{s,2}}{\partial y}}{\frac{\partial \widetilde{T}_{s,1}}{\partial y}} \exp\left(\alpha \Delta \widetilde{T}_s\right). \tag{11}$$

414

415   Thus, to more cleanly separate thermodynamic from dynamic influences on the LHC, we

416 introduce the LHC scaling. This scaling is independent of the budget analysis of Section 4a and

417 derives from the semi-empirical linear relationship between wet (dry) LHC and moist (dry) wave

418 activity. This relationship, found for the moist and total wave activities by L17 and L18, also

419 extends to the dry, and it is expressed as

420
$$(\widetilde{P-E})^+ \sim \frac{A^+ - A_c^+}{\tau^+} \tag{12a}$$

421
$$(\widetilde{E-P})^- \sim \frac{A^-}{\tau^-}. \tag{12b}$$

422 Here A_c^+ is the critical amplitude (Supplemental Figure 4), defined as the minimum amplitude

423 required of a moist intrusion to participate in the wet LHC. It is calculated as the intercept in the

424 linear regression between A^+ and $(\widetilde{P-E})^+$ (L17; Xue et al. 2018). The intercept is negligible for

425 the dry regression, implying dry waves do not need a critical amplitude. (This asymmetry is

426 analogous to ascent and descent, the latter always being unsaturated.) The other important

427 scaling factor here is τ, which represents the timescale over which moist and dry intrusions are

428 damped by their respective sinks (Supplemental Figure 4). Since the LHC acts as a wave activity

429 forcing on short time scales [$\frac{\partial A}{\partial t}$, see (4)], τ can be understood as an approximate e-folding

430 relaxation time for the wet LHC to return wave activity to its critical amplitude and the dry LHC

431 to return wave activity to the background state.

22

432   When calculating the above regression, we first aggregate the $1.25° \times \sim1°$ data into

433    $7.5° \times \sim6°$ degree data (using six-by-six blocks of the original grid as the new grid cell) because

434   the strength of the linear relationship between A and $(\widetilde{E - P})$ comes in part from the central

435   limit theorem (L17). For most grid cells, this brings enough "normality" to justify the linear

436   regression; aggregating over larger areas does not substantially improve performance (not

437   shown). Because the choice of independent variable in the regression is arbitrary, we utilize

438   reduced major-axis regression (see L17 and references therein). When displaying the timescale

439   and critical amplitude, we interpolate back to the original $1.25° \times 1°$ grid for consistency with

440   the mixing length.

441   To remove the thermodynamic effects of the moisture gradient, the wave activity in (12)

442   can be scaled like a wave amplitude as $A^+ \sim m_e^+ \eta^+ \sim \frac{\partial M}{\partial y}(\eta^+)^2$ or $A^- \sim m_e^- \eta^- \sim \frac{\partial M}{\partial y}(\eta^-)^2$ (L17),

443   where η is the mixing length. Combining this with (12) yields the scaling for the wet or dry LHC:

444
$$(\widetilde{P - E})^+ \sim \frac{\partial M}{\partial y}\frac{A^+ - A_c^+}{A^+}\frac{(\eta^+)^2}{\tau^+} \tag{13a}$$

445
$$(\widetilde{E - P})^- \sim \frac{\partial M}{\partial y}\frac{(\eta^-)^2}{\tau^-}, \tag{13b}$$

446   Or, in its fractional form:

447
$$\frac{\delta(\widetilde{P - E})^+}{(\widetilde{P - E})^+} \sim \frac{\delta\left(\frac{\partial M}{\partial y}\right)}{\frac{\partial M}{\partial y}} + 2\frac{\delta\eta^+}{\eta^+} + \frac{\delta(\tau^+)^{-1}}{(\tau^+)^{-1}} + \frac{\delta\left(\frac{A^+ - A_c^+}{A^+}\right)}{\frac{A^+ - A_c^+}{A^+}} \tag{14a}$$

23

448
$$\frac{\delta(\widetilde{E-P})^-}{(\widetilde{E-P})^-} \sim \frac{\delta\left(\frac{\partial M}{\partial y}\right)}{\frac{\partial M}{\partial y}} + 2\frac{\delta\eta^-}{\eta^-} + \frac{\delta(\tau^-)^{-1}}{(\tau^-)^{-1}}. \qquad (14b)$$

449   Intuitively, the scaling suggests changes in wet and dry extremes are driven by 1) a

450   changing background moisture gradient, 2) a changing mixing length scale, and 3) a changing

451   cycling rate (τ^{-1}). In addition, the wet LHC (14a) may also be influenced by changes in the

452   quantity $\left(\frac{A^+ - A_c^+}{A^+}\right)$, termed the participation ratio, which reflects the portion of a moist intrusion

453   exceeding the critical amplitude and thus being damped by ("participating in") the wet LHC.

454   Absent the participation ratio, the scaling in (13) has a similar form to other diffusive scalings of

455   the eddy moisture flux (c.f., Caballero and Hanley 2012), whose vertical integral largely

456   balances precipitation.

457   The mixing length η we define here is thus qualitatively similar to Eulerian estimates as a

458   measure of the effective displacement of column-mean moisture by large-scale eddies, which is

459   related to the width of the baroclinically unstable zone (particularly for the moist mixing

460   length). Crucially, however, the moist and dry mixing lengths measure displacement from the

461   wave-free, conservatively-estimated background state M rather than the zonal-mean. Since the

462   zonal-mean CWV decreases poleward more gradually than the background state, this generally

463   results in a longer (but similar order of magnitude) estimate of mixing length compared to other

464   estimates (c.f. Caballero and Hanley 2012, Swanson and Pierrehumbert 1997, Tandon et al.

465   2018). Further, the adiabatic assumption which guides the construction of the background state

466   (Nakamura and Solomon 2010) may result in longer mixing lengths than those accounting for

467   strong diabatic effects (Caballero and Hanley 2012). Despite these differences in definition, the

24

468   mixing length utilized for the LHC plays a large role in the magnitude and spatial distribution of

469   the LHC's dynamic response since it is the only quadratic term in the scaling. Thus, it provides

470   important insight into how large-scale moisture transport processes driven by eddy stirring can

471   modify the LHC.

472   Before analyzing the dynamic changes in the LHC in detail, we first verify the

473   thermodynamic scalings for the background state and gradient (Figure 5). CWV background

474   scaling is evaluated in Figure 5a, where we use a slight modification of (10) to predict the future

475   CWV background distribution (M_2) given the present-day quantities (subscript 1), present-day

476   and RCP8.5 zonal-mean temperature, and an Earth-like $\alpha = 7.4\%/K$ (O'Gorman and Muller

477   2010; Lorenz and DeWeaver 2007). We calculate the present-day CWV-associated temperature

478   as the surface temperature along a CWV contour [$\widetilde{T}_s \equiv \widetilde{T}_s(\phi_e)$], and we approximate the future

479   CWV-associated temperature by multiplying its present distribution with the ratio of the RCP8.5

480   to present-day zonal-mean temperatures ($\widetilde{T_{s,2}} \approx \widetilde{T_{s,1}} \frac{T_{s,2}}{T_{s,1}}$). This ensures we are not unfairly

481   utilizing the future CWV distribution to predict the background state CWV.

482   Overall, the scaling performs quite well for most latitudes for the background state

483   (Figure 5a), which monotonically decreases moving poleward by construction. The scaling

484   modestly underpredicts the background CWV near the equator, where CWV-associated

485   temperature is not well-defined, and it overpredicts the background CWV in the Northern

486   Hemisphere high latitudes. The scaling likely overpredicts here because the assumption of

487   constant CWV saturation fraction (σ) holds less well over land than ocean (i.e., Byrne and

488   O'Gorman 2015).

25

489   Despite the approximations required to compute gradients numerically on a coarse grid,

490   we successfully predict the future gradient (Figure 5b) using (11) in the same manner as we

491   used (10) to predict the background state. This demonstrates that the sharpening moisture

492   gradient is fundamentally a thermodynamic response. The gradient scaling also does not

493   accurately predict changes near the equator (where the gradient is poorly defined) or in the

494   high latitude Northern Hemisphere, likely for the same reason the background state scaling

495   overpredicts changes in this region.

496   Instead of using a fixed rate α to predict future changes, we also compute it directly to

497   evaluate the degree to which RCP8.5 changes obey the CC relation. This "CC rate" is like a

498   fractional rate of change except it accounts for the exponential scaling of the CC relation

499   (O'Gorman and Muller 2010). It increases relatively uniformly, with most regions hovering

500   around $7.5\%/K$ (Figure 5c). In contrast, the CC rate for Eulerian zonal-mean CWV is more

501   variable with latitude (black dashed line). Thus, we argue that M is better constrained by CC-

502   scaling than its Eulerian counterpart and is an effective measure of thermodynamic impacts.

503   The fractional changes in gradient fluctuate meridionally considerably more than the changes in

504   the CWV background, but as we have shown the changes are essentially thermodynamic.

505   We proceed to use the LHC scaling to examine the LHC structure for the present-day

506   annual-mean (Figure 6), beginning with the mixing length. The mixing length is calculated by

507   directly computing the displacement of the M contour from its equivalent latitude. The

508   present-day moist mixing length scale (Figure 6a) is long on the equatorward flanks of storm

509   tracks and in monsoon regions, reflecting how these circulations transport moisture, both

510   directly and indirectly through enhanced wave-breaking. The dry mixing length scale is largest

26

511   in the subtropics (Figure 6b), as the large values poleward of orography are likely artefacts from

512   the orographic "dry island" effect (see Section 3). Interestingly, the dry mixing length scale

513   exhibits local maxima over North Africa, the Western United States, and Australia, while the dry

514   LHC is generally small over land (Figure 2b) due to the soil moisture constraint on evaporation.

515   The moist cycling rate (Figure 6c) increases from very low values in the subtropics (long

516   moist time scale) to high values in the polar regions (short moist time scale), especially near

517   orography. In contrast, the dry cycling rate (Figure 6d) is very low in the tropics, likely because

518   upward motion in convective regions is stronger than downward motion (Bretherton et al.

519   2005) which leads to longer dry wave lifetimes. Both cycling rates tend to be strongest in the

520   vicinity of storm tracks, particularly in jet entrance and exit regions, where wave breaking leads

521   to mixing and brief wave lifetimes.

522   The present-day structure of the participation ratio (Figure 6e) can be understood by

523   considering the critical amplitude. In the tropics, where the critical amplitude is kept low by

524   deep convection, the participation ratio is high. It decreases rapidly into the subtropics, where a

525   large critical amplitude favors the transport of wave activity rather than its conversion into

526   precipitation. This minimum participation ratio is critical for transport by AR, which is examined

527   further in Section 4c. Storm track regions also exhibit local maxima in the participation ratio, as

528   the increased baroclinicity reduces the critical amplitude (Xue et al. 2018).

529   Now we use (14) to decompose RCP8.5 changes in the LHC. Overall, the cumulative

530   scaling contributions match the spatial pattern of changes quite well, with some overestimation

531   of their magnitude, particularly in the dry case (Supplemental Figure 3). Changes in mixing

27

532   length scale (Figure 7a,b) again paint a picture of dynamically-driven drying in the subtropics

533   and midlatitudes, with increases in dry length scale and decreases in moist length scale,

534   consistent with the weakened midlatitude stirring found by L17. A notable exception to this is

535   over the Southern Ocean and to an extent the North Pacific, consistent with projections of

536   intensified storm tracks (Chang et al. 2012). Advective contributions to the LHC budget (Figure

537   4e-h) support this notion. Comparing with climatology (Figure 6a,b), length scale changes also

538   suggest a poleward shift of storm tracks, which is more consistent with previous findings than

539   the results from the budget-based decomposition.

540   Changes in the hydrological cycling rate portray an increasing residence time

541   (decreasing rate) for moist waves (Figure 7c; brown shading), consistent with but more general

542   than the slowdown of the general circulation predicted by earlier work (e.g., Held and Soden

543   2006; Vecchi and Soden 2007). This result is consistent with L18, who attribute the change to a

544   weakening of vertical motion or an upward shift of the atmospheric circulation (Singh and

545   O'Gorman 2012). Likewise, residence times decrease for dry waves in almost all regions (Figure

546   7d; green shading) except the deep tropics. A possible explanation for the decreasing lifetime

547   for dry waves is the weakening of downward vertical motions by the increasing dry static

548   stability (Tamarin-Brodsky and Hadas 2019).

549   The participation ratio (Figure 7e) decreases in most regions (brown shading). This may

550   be due to the increase in the atmospheric moisture storage capacity, which gives rise to a

551   smaller fraction of moist waves which condense into precipitation. An important exception

552   occurs near the North Atlantic warming hole. In this region, cooler SST lead to strong growth in

553   moist wave damping and an increase in the LHC. This interpretation is supported by the large

28

554   increases in the NA which are seen in the zonal moist LWA flux convergence (Figure 4g). As a

555   reference, the fractional change in moisture gradient from Figure 5c is shown again (Figure 7f),

556   normalized by global-mean temperature, as it contributes positively towards both ends of the

557   LHC.

558

559   *c. Implications for Atmospheric Rivers*

560   Beyond providing a clean separation between dynamic and thermodynamic

561   components, this scaling can be further utilized to probe moisture transport, particularly AR.

562   Crucially, the scaling reveals that a moist intrusion is not entirely available for participation in

563   the wet LHC, as some proportion of it (measured by one minus the participation ratio, or $1 -$

564     $\frac{A^+ - A_c^+}{A^+} \equiv \frac{A_c^+}{A^+}$) must be reserved due to energetic limitations and the temperature dependence of

565   saturation. Thus, the critical amplitude A_c^+ measures the moisture transport by intrusions which

566   does not result in precipitation. Because the non-precipitating portion of AR are characterized

567   by large wave activity and low participation ratio (L17), A_c^+ has important implications for

568   moisture transport by AR. This picture of the wet LHC is akin to a watershed with a dam

569   controlling its outlet (Figure 8).

570   In this analogy, the moist wave activity measures the amount of water in the watershed.

571   Any influx of water (wave activity) into the watershed which exceeds the capacity of the dam,

572   which represents the critical amplitude, must be released from the watershed. This released

573   fraction of the water constitutes the wet LHC, and the rate the dam releases water is the cycling

574   rate. Just as an understanding of a watershed's outlet would be incomplete without examining

29

575   the regulating reservoir, this analogy suggests our understanding of the active LHC could be

576   furthered by examining the critical amplitude.

577   To accomplish this, we utilize a scaling for the critical amplitude similar to the moist

578   wave activity $A^+ \sim \frac{\partial M}{\partial y}(\eta^+)^2$:

$$A_c^+ \sim \frac{\partial M}{\partial y}(\eta_c^+)^2. \tag{15}$$

580   Here, η_c^+ takes on the meaning of "mean free path", or the distance moist waves can propagate

581   with their humidity content conserved (L17). Thus, it resembles estimates of mixing length

582   which rely on tracer conservation, such as meridional velocity autocorrelation (e.g., Swanson

583   and Pierrehumbert 1997, Caballero and Hanley 2012). However, it is longer than these other

584   estimates, just as the moist and dry mixing lengths were, and for the same reasons. Similarly to

585   the mixing length, the mean free path represents the dynamic contribution to changes in the

586   critical amplitude.

587   As previously mentioned, we calculate the critical amplitude as the intercept from the

588   regression in (12a), and we subsequently use (15) to calculate the mean free path. The present-

589   day critical amplitude in CESM LENS (Figure 9a) highlights source regions for AR where moisture

590   transport exceeds moisture loss via condensation, such as the Western Pacific and North

591   Atlantic, as we would expect. While AR are not stationary like the reservoirs in our analogy,

592   they are the dominant meridional moisture transporters (Zhu and Newell 1998) and are

593   inefficient precipitators (L17; L18), making them the major contributors to the critical

30

594 amplitude. However, the critical amplitude is not capturing AR impacts, as it is distinct from the

595 LHC which results in (net) precipitation.

596   Under RCP8.5, the critical amplitude (Figure 9b) increases in a like fashion to the wet

597 LHC (Figure 2b), excepting smaller decreases in the subtropics and larger increases near the

598 poles. Despite showing a strong increase in the wet LHC (Figure 2b), the North Atlantic region

599 shows a modest decrease in the reserved LHC, which may partially explain the increase in the

600 active portion (if one assumes the total LHC does not change significantly in this region).

601   The present-day mean free path (Figure 9c) is longest in jet entrance and exit regions,

602 illustrating how large-scale wave breaking transports moisture by stretching material contours

603 and elongating the mean free path. The present-day mean free path is particularly large over

604 the North Atlantic, where the strong, wintertime storm track excels at transporting moisture

605 from near the subtropics into the Arctic (Supplemental Figure 5), and over the northern Indian

606 Ocean and northwest Pacific, where summertime monsoonal circulations are the dominant

607 moisture transporters (Supplemental Figure 6; Xue et al. 2018). The mean-free path is large

608 over continental interiors during the summer season, perhaps reflective of the role of low-level

609 jets (Algarra et al. 2019).

610   While the critical amplitude generally increases in a warmer climate, RCP8.5 changes in

611 mean free path (Figure 9d) show a decrease in subtropical regions and an increase in higher

612 latitudes. A crucial exception to this high-latitude lengthening is in the North Atlantic near the

613 warming hole. This unravels the dynamics behind the super-CC increase seen in the wet LHC

614 here (Figure 1b): the cooler SST act to enhance condensation, reduce the mean free path, lower

615　the critical amplitude, and thereby raise the participation ratio (Figure 7e), which is the central

616　dynamic contributor. This is consistent with the previous budget-based results (Figure 4g) that

617　the warming hole results in a locally-sharpened SST gradient, enhancing baroclinicity and the

618　participation ratio, and also increasing the downstream convergence of moist wave activity.

619　　　　Changes in mean free path (Figure 9d) also explain the subtropical decreases in the

620　critical amplitude (Figure 9b), which is consistent with a weakened stirring (L17). Whether this

621　decline will exceed the thermodynamically-driven increase appears to underlie the ensemble

622　uncertainty in critical amplitude (stippling, Figure 9b). As with uncertainty in the moist mixing

623　length (Figure 7a), the uncertainty in mean free path (stippling, Figure 9d) is largely at the

624　margins of the subtropical decline, implicating the strength of the expansion as the source of

625　uncertainty. This result further emphasizes the profound impacts of subtropical expansion on

626　the LHC, suggesting that further insight into dynamic LHC changes should focus on the impacts

627　of subtropical change on wave breaking and moisture transport.

628

629　**5.　Summary and Conclusions**

630　　　　Here we have conducted a thorough analysis of changes in the local hydrologic cycle

631　(LHC) for the RCP8.5 scenario as simulated by the CESM1 Large Ensemble (LENS). Our dynamical

632　approach provides two independent methods for decomposing wet and dry LHC changes, with

633　contributions either from overturning and advective circulations, or from the moisture gradient,

634　mixing length, and cycling rate (and participation ratio for the moist case). We show the

635　thermodynamic changes measured here are commensurate with the Clausius-Clapeyron

32

636   relation. To the first order, changes in tropical LHC are due to thermodynamic increases

637   countered by weakening low-level convergence, likely due to the slowdown of the Hadley

638   circulation (Lu et al. 2007; Vecchi and Soden 2007) and increasing land-sea contrast (He and

639   Soden 2017).

640   In the mid-latitudes, wet LHC changes are driven by thermodynamic increases in

641   conjunction with increasing meridional advection. This advection primarily results from

642   extratropical cyclones and atmospheric rivers, pointing to the need for a robust understanding

643   of midlatitude storm track changes. The dominant pattern of dry LHC changes is one of

644   subtropical expansion. These changes are mainly driven by changes in overturning and in the

645   zonal dry LWA flux divergence, the latter being key in jet entrance and exit regions.

646   Our scaling-based approach further reveals a global slowdown in the LHC cycling rate,

647   along with a shortened moist mixing length but a lengthened dry mixing length for the

648   midlatitudes. These changes appear linked to subtropical expansion and changes in stability,

649   which also reduce the moisture mean free path.

650   Based on this analysis, we argue that the meridional shift and weakening of the general

651   circulation is the predominant dynamic driver behind the intensifying LHC in CESM LENS. While

652   we do not neglect the importance of different regionally relevant mechanisms, we can quantify

653   their relative and synthetic contributions and directly link changes in the LHC to changes in

654   different circulation regimes. This suggests that ongoing efforts to predict and constrain

655   circulation changes may ultimately help constrain annual changes in the mean hydrologic cycle

656   and the extremes (Shepherd 2014; Pfahl et al. 2017).

657   We now suggest several avenues for future work. The dry LHC budget analysis

658   presented here is a unique contribution of this work, but the presence of strong artefacts over

659   the land surface makes it difficult to interpret for many important regions. Future work should

660   seek to minimize the numerical impacts of orography on the dry LHC. Changes in dryness are

661   often considered on longer time scales than the six-hourly changes analyzed here (Polade et al.

662   2014), which creates a challenge for contextualizing these results. Yet the changes in the dry

663   LHC over the ocean modestly resemble the spatial patterns of change seen in changes in dry

664   days (Polade et al. 2014), increasing our confidence in the relevance of these results.

665   Ongoing extension of this work will analyze CMIP6 models to identify the robust

666   dynamic contributions to the LHC change under global warming and the dynamical sources of

667   intermodel spread. Future work will begin by evaluating models against these results and

668   against reanalysis to identify dynamic sources of climatological bias. These dynamic

669   contributors will then be compared to reanalysis data to further evaluate the simulated

670   interactions between the large-scale circulation and the hydrologic cycle.

671

34

682   **Data Availability**

683   The six-hourly CESM LENS data were downloaded from the National Center for

684   Atmospheric Research and are publicly available upon request. Code for computing the wave

685   activity budget is available from the corresponding author upon request.

686

687   **References**

688   Algarra, I., J. Eiras-Barca, R. Nieto, and L. Gimeno, 2019: Global climatology of nocturnal low-

689   level jets and associated moisture sources and sinks. *Atmospheric Res.*, **229**, 39–59,

690   https://doi.org/10.1016/j.atmosres.2019.06.016.

691   Allen, M. R., and W. J. Ingram, 2002: Constraints on future changes in climate and the

692   hydrologic cycle. *Nature*, **419,** 228-232, doi:10.1038/nature01092.

693   Bony, S., G. Bellon, D. Klocke, S. Sherwood, S. Fermepin, and S. Denvil, 2013: Robust direct

694   effect of carbon dioxide on tropical circulation and regional precipitation. *Nature

695   Geoscience*, **6,** 447-451, doi:10.1038/ngeo1799.

696   Bretherton, C. S., P. N. Blossey, and M. Khairoutdinov, 2005: An Energy-Balance Analysis of

697   Deep Convective Self-Aggregation above Uniform SST. *J. Atmos. Sci.*, **62**, 4273–4292,

698   https://doi.org/10.1175/JAS3614.1.

699   Byrne, M. P., and P. A. O'Gorman, 2013: Land–Ocean Warming Contrast over a Wide Range of

700   Climates: Convective Quasi-Equilibrium Theory and Idealized Simulations. *Journal of*

701   *Climate*, **26,** 4000-4016, doi:10.1175/JCLI-D-12-00262.1.

702   Byrne, M. P., and P. A. O'Gorman, 2015: The Response of Precipitation Minus

703   Evapotranspiration to Climate Warming: Why the "Wet-Get-Wetter, Dry-Get-Drier"

704   Scaling Does Not Hold over Land. *J. Climate*, **28**, 8078–8092,

705   https://doi.org/10.1175/JCLI-D-15-0369.1.

706   Caballero, R., and J. Hanley, 2012: Midlatitude Eddies, Storm-Track Diffusivity, and Poleward

707   Moisture Transport in Warm Climates. *Journal of the Atmospheric Sciences*, **69**, 3237–

708   3250, https://doi.org/10.1175/JAS-D-12-035.1.

709   Chang, E. K. M., Y. Guo, and X. Xia, 2012: CMIP5 multimodel ensemble projection of storm track

710   change under global warming. *Journal of Geophysical Research: Atmospheres*, **117**,

711   doi:10.1029/2012jd018578.

712   Chen, G., J. Norris, J. D. Neelin, J. Lu, L. R. Leung, and K. Sakaguchi, 2019: Thermodynamic and

713   Dynamic Mechanisms for Hydrological Cycle Intensification over the Full Probability

714   Distribution of Precipitation Events. *Journal of the Atmospheric Sciences*, **76,** 497-516,

715   doi:10.1175/jas-d-18-0067.1.

716 Fahad, A. al, N. J. Burls, and Z. Strasberg, 2020: How will southern hemisphere subtropical

717   anticyclones respond to global warming? Mechanisms and seasonality in CMIP5 and

718   CMIP6 model projections. *Clim. Dyn.*, **55**, 703–718, https://doi.org/10.1007/s00382-020-

719   05290-7.

720 Feng, X., C. Liu, F. Xie, J. Lu, L. S. Chiu, G. Tintera, and B. Chen, 2019: Precipitation characteristic

721   changes due to global warming in a high-resolution (16 km) ECMWF

722   simulation. *Quarterly Journal of the Royal Meteorological Society*, **145,** 303-317,

723   doi:10.1002/qj.3432.

724 Gao, Y., J. Lu, L. R. Leung, Q. Yang, S. Hagos, and Y. Qian, 2015: Dynamical and thermodynamical

725   modulations on future changes of landfalling atmospheric rivers over western North

726   America. *Geophysical Research Letters*, **42,** 7179-7186, doi:10.1002/2015gl065435.

727 Hagos, S. M., L. R. Leung, J.-H. Yoon, J. Lu, and Y. Gao, 2016: A projection of changes in

728   landfalling atmospheric river frequency and extreme precipitation over western North

729   America from the Large Ensemble CESM simulations. *Geophysical Research*

730   *Letters*, **43,** 1357-1363, doi:10.1002/2015gl067392.

731 He, C., B. Wu, L. Zou, and T. Zhou, 2017: Responses of the Summertime Subtropical

732   Anticyclones to Global Warming. *J. Clim.*, **30**, 6465–6479, https://doi.org/10.1175/JCLI-

733   D-16-0529.1.

734 He, J., and B. J. Soden, 2017: A re-examination of the projected subtropical precipitation

735   decline. *Nature Climate Change*, **7**, 53–57, https://doi.org/10.1038/nclimate3157.

736   Held, I. M., and B. J. Soden, 2000: Water Vapor Feedback and Global Warming. *Annu. Rev.*

737   *Energy. Environ.*, **25**, 441–475, https://doi.org/10.1146/annurev.energy.25.1.441.

738   Held, I. M., and B. J. Soden, 2006: Robust Responses of the Hydrological Cycle to Global

739   Warming. *Journal of Climate*, **19,** 5686-5699, doi:10.1175/jcli3990.1.

740   Huang, C. S. Y., and N. Nakamura, 2016: Local Finite-Amplitude Wave Activity as a Diagnostic of

741   Anomalous Weather Events. *Journal of the Atmospheric Sciences*, **73,** 211-229,

742   doi:10.1175/jas-d-15-0194.1.

743   ——, 2017: Local wave activity budgets of the wintertime Northern Hemisphere: Implication for

744   the Pacific and Atlantic storm tracks. *Geophysical Research Letters*, **44,** 5673-5682,

745   doi:10.1002/2017gl073760.

746   Huang, P., D. Chen, and J. Ying, 2017: Weakening of the Tropical Atmospheric Circulation

747   Response to Local Sea Surface Temperature Anomalies under Global Warming. *Journal*

748   *of Climate*, **30,** 8149-8158, doi:10.1175/JCLI-D-17-0171.1.

749   Joshi, M. M., J. M. Gregory, M. J. Webb, D. M. H. Sexton, and T. C. Johns, 2008: Mechanisms for

750   the land/sea warming contrast exhibited by simulations of climate change. *Climate*

751   *Dynamics*, **30,** 455-465, doi:10.1007/s00382-007-0306-1.

752   Kang, S. M., and J. Lu, 2012: Expansion of the Hadley Cell under Global Warming: Winter versus

753   Summer. *Journal of Climate*, **25,** 8387-8393, doi:10.1175/JCLI-D-12-00323.1.

754   Kay, J. E., and Coauthors, 2014: The Community Earth System Model (CESM) Large Ensemble

755   Project: A Community Resource for Studying Climate Change in the Presence of Internal

756   Climate Variability. *Bulletin of the American Meteorological Society*, **96,** 1333-1349,

757   doi:10.1175/BAMS-D-13-00255.1.

758 Kim, B.-M., and Coauthors, 2014: Weakening of the stratospheric polar vortex by Arctic sea-ice

759   loss. *Nature Communications*, **5,** 4646, doi: 10.1038/ncomms5646.

760 Liu, B., X. Tan, T. Y. Gan, X. Chen, K. Lin, M. Lu, and Z. Liu, 2020: Global atmospheric moisture

761   transport associated with precipitation extremes: Mechanisms and climate change

762   impacts. *WIREs Water*, **7,** e1412, doi: 10.1002/wat2.1412.

763 Lorenz, D. J., and E. T. DeWeaver, 2007: The Response of the Extratropical Hydrological Cycle to

764   Global Warming. *Journal of Climate*, **20,** 3470-3484, doi:10.1175/JCLI4192.1.

765 Lu, J., G. A. Vecchi, and T. Reichler, 2007: Expansion of the Hadley cell under global

766   warming. *Geophysical Research Letters*, **34,** doi:10.1029/2006gl028443.

767 Lu, J., and Coauthors, 2014: The robust dynamical contribution to precipitation extremes in

768   idealized warming simulations across model resolutions. *Geophysical Research*

769   *Letters*, **41,** 2971-2978, doi:10.1002/2014GL059532.

770 Lu, J., and Coauthors, 2017: Examining the Hydrological Variations in an Aquaplanet World

771   Using Wave Activity Transformation. *Journal of Climate*, **30,** 2559-2576, doi:10.1175/jcli-

772   d-16-0561.1.

773 Lu, J., D. Xue, Y. Gao, G. Chen, L. R. Leung, and P. Staten, 2018: Enhanced hydrological extremes

774   in the western United States under global warming through the lens of water vapor

775   wave activity. *npj Climate and Atmospheric Science*, **1,** 7, doi:10.1038/s41612-018-0017-

776   9.

777 Menary, M. B., and R. A. Wood, 2018: An anatomy of the projected North Atlantic warming

778   hole in CMIP5 models. *Climate Dynamics*, **50,** 3063-3080, doi:10.1007/s00382-017-3793-

779   8.

780 Nakamura, N., and A. Solomon, 2010: Finite-Amplitude Wave Activity and Mean Flow

781   Adjustments in the Atmospheric General Circulation. Part I: Quasigeostrophic Theory

782   and Analysis. *Journal of the Atmospheric Sciences*, **67,** 3967-3983,

783   doi:10.1175/2010jas3503.1.

784 Neelin, J. D., B. Langenbrunner, J. E. Meyerson, A. Hall, and N. Berg, 2013: California Winter

785   Precipitation Change under Global Warming in the Coupled Model Intercomparison

786   Project Phase 5 Ensemble. *Journal of Climate*, **26,** 6238-6256, doi:10.1175/jcli-d-12-

787   00514.1.

788 Neelin, J. D., and Coauthors, 2010: Long tails in deep columns of natural and anthropogenic

789   tropospheric tracers. *Geophysical Research Letters*, **37**, doi:10.1029/2009gl041726.

790 O'Gorman, P. A., 2015: Precipitation Extremes Under Climate Change. *Current Climate Change*

791   *Reports*, **1,** 49-59, doi:10.1007/s40641-015-0009-3.

792 O'Gorman, P. A., and C. J. Muller, 2010: How closely do changes in surface and column water

793   vapor follow Clausius–Clapeyron scaling in climate change simulations? *Environmental*

794   *Research Letters*, **5**, doi:10.1088/1748-9326/5/2/025207.

795   O'Gorman, P. A., and T. Schneider, 2009: The physical basis for increases in precipitation

796   extremes in simulations of 21st-century climate change. *Proceedings of the National*

797   *Academy of Sciences*, **106,** 14773-14777, doi:10.1073/pnas.0907610106.

798   Peings, Y., J. Cattiaux, S. Vavrus, and G. Magnusdottir, 2017: Late Twenty-First-Century Changes

799   in the Midlatitude Atmospheric Circulation in the CESM Large Ensemble. *Journal of*

800   *Climate*, **30,** 5943-5960, doi:10.1175/jcli-d-16-0340.1.

801   Pendergrass, A. G., and E. P. Gerber, 2016: The Rain Is Askew: Two Idealized Models Relating

802   Vertical Velocity and Precipitation Distributions in a Warming World. *Journal of*

803   *Climate*, **29,** 6445-6462, doi:10.1175/jcli-d-16-0097.1.

804   Pfahl, S., P. A. O'Gorman, and E. M. Fischer, 2017: Understanding the regional pattern of

805   projected future changes in extreme precipitation. *Nature Climate Change*, **7,** 423-427,

806   doi:10.1038/nclimate3287.

807   Polade, S. D., D. W. Pierce, D. R. Cayan, A. Gershunov, and M. D. Dettinger, 2014: The key role

808   of dry days in changing regional climate and precipitation regimes. *Scientific*

809   *Reports*, **4,** 4364, doi:10.1038/srep04364.

810   Polade, S. D., A. Gershunov, D. R. Cayan, M. D. Dettinger, and D. W. Pierce, 2017: Precipitation

811   in a warming world: Assessing projected hydro-climate changes in California and other

812   Mediterranean climate regions. *Scientific Reports*, **7,** 10783, doi:10.1038/s41598-017-

813   11285-y.

814   Romanowsky, E., and Coauthors, 2019: The role of stratospheric ozone for Arctic-midlatitude

815   linkages. *Scientific Reports*, **9,** 7962, doi: 10.1038/s41598-019-43823-1.

816   Scheff, J., and D. M. W. Frierson, 2012: Robust future precipitation declines in CMIP5 largely

817   reflect the poleward expansion of model subtropical dry zones. *Geophys. Res. Lett.*, **39**,

818   https://doi.org/10.1029/2012gl052910.

819   ——, 2014: Scaling Potential Evapotranspiration with Greenhouse Warming. *Journal of*

820   *Climate*, **27,** 1539-1558, doi:10.1175/JCLI-D-13-00233.1.

821   Seager, R., N. Naik, and G. A. Vecchi, 2010: Thermodynamic and Dynamic Mechanisms for

822   Large-Scale Changes in the Hydrological Cycle in Response to Global Warming. *Journal of*

823   *Climate*, **23,** 4651-4668, doi:10.1175/2010JCLI3655.1.

824   Seager, R., and N. Henderson, 2013: Diagnostic Computation of Moisture Budgets in the ERA-

825   Interim Reanalysis with Reference to Analysis of CMIP-Archived Atmospheric Model

826   Data. *Journal of Climate*, **26**, 7876–7901, https://doi.org/10.1175/JCLI-D-13-00018.1.

827   Shaw, T. A., 2019: Mechanisms of Future Predicted Changes in the Zonal Mean Mid-Latitude

828   Circulation. *Current Climate Change Reports*, **5,** 345-357, doi: 10.1007/s40641-019-

829   00145-8.

830   Shaw, T. A., and Coauthors, 2016: Storm track processes and the opposing influences of climate

831   change. *Nature Geoscience*, **9,** 656-664, doi: 10.1038/ngeo2783.

832   Shepherd, T. G., 2014: Atmospheric circulation as a source of uncertainty in climate change

833   projections. *Nature Geoscience*, **7,** 703, doi:10.1038/ngeo2253.

42

834   Singh, M. S., and P. A. O'Gorman, 2012: Upward Shift of the Atmospheric General Circulation

835   under Global Warming: Theory and Simulations. *Journal of Climate*, **25,** 8259-8276,

836   doi:10.1175/JCLI-D-11-00699.1.

837   Song, F., L. R. Leung, J. Lu, and L. Dong, 2018: Seasonally dependent responses of subtropical

838   highs and tropical rainfall to anthropogenic warming. *Nature Climate Change*, **8,** 787-

839   792, doi:10.1038/s41558-018-0244-4.

840   Staten, P. W., K. M. Grise, S. M. Davis, K. Karnauskas, and N. Davis, 2019: Regional Widening of

841   Tropical Overturning: Forced Change, Natural Variability, and Recent Trends. *Journal of*

842   *Geophysical Research: Atmospheres*, **124,** 6104-6119, doi: 10.1029/2018jd030100.

843   Stephens, G. L., and Y. Hu, 2010: Are climate-related changes to the character of global-mean

844   precipitation predictable? *Environmental Research Letters*, **5,** 025209,

845   doi:10.1088/1748-9326/5/2/025209.

846   Swanson, K. L., and R. T. Pierrehumbert, 1997: Lower-Tropospheric Heat Transport in the Pacific

847   Storm Track. *Journal of the Atmospheric Sciences*, **54**, 1533–1543,

848   https://doi.org/10.1175/1520-0469(1997)054<1533:LTHTIT>2.0.CO;2.

849   Tamarin-Brodsky, T., and O. Hadas, 2019: The Asymmetry of Vertical Velocity in Current and

850   Future Climate. *Geophysical Research Letters*, **46,** 374-382, doi:10.1029/2018gl080363.

851   Tamarin-Brodsky, T., and Y. Kaspi, 2017: Enhanced poleward propagation of storms under

852   climate change. *Nature Geoscience*, **10**, 908–913, https://doi.org/10.1038/s41561-017-

853   0001-8.

43

854   Tandon, N. F., X. Zhang, and A. H. Sobel, 2018: Understanding the Dynamics of Future Changes

855   in Extreme Precipitation Intensity. *Geophysical Research Letters*, **45,** 2870-2878,

856   doi:10.1002/2017gl076361.

857   Thackeray, C. W., A. M. DeAngelis, A. Hall, D. L. Swain, and X. Qu, 2018: On the Connection

858   Between Global Hydrologic Sensitivity and Regional Wet Extremes. *Geophysical*

859   *Research Letters*, **45,** 11,343-311,351, doi: 10.1029/2018gl079698.

860   Trenberth, K. E., 1999: Conceptual Framework for Changes of Extremes of the Hydrological

861   Cycle with Climate Change. *Climatic Change*, **42,** 327-339,

862   doi:10.1023/A:1005488920935.

863   Trenberth, K. E., and C. J. Guillemot, 1995: Evaluation of the Global Atmospheric Moisture

864   Budget as Seen from Analyses. *Journal of Climate*, **8,** 2255-2272, doi:10.1175/1520-

865   0442(1995)008<2255:eotgam>2.0.co;2.

866   Vallis, G. K., 2006: *Atmospheric and Oceanic Fluid Dynamics*. 1st ed. Cambridge University Press,

867   770 pp.

868   Vecchi, G. A., and B. J. Soden, 2007: Global Warming and the Weakening of the Tropical

869   Circulation. *J. Clim.*, **20**, 4316–4340, https://doi.org/10.1175/JCLI4258.1.

870   Weller, E., C. Jakob, and M. J. Reeder, 2019: Understanding the Dynamic Contribution to Future

871   Changes in Tropical Precipitation From Low-Level Convergence Lines. *Geophysical*

872   *Research Letters*, **46,** 2196-2203, doi:10.1029/2018gl080813.

873   Wills, R. C., M. P. Byrne, and T. Schneider, 2016: Thermodynamic and dynamic controls on

874   changes in the zonally anomalous hydrological cycle. *Geophys. Res. Lett.*, **43**, 4640–

875   4649, https://doi.org/10.1002/2016GL068418.

876   Xue, D., J. Lu, L. R. Leung, and Y. Zhang, 2018: Response of the Hydrological Cycle in Asian

877   Monsoon Systems to Global Warming Through the Lens of Water Vapor Wave Activity

878   Analysis. *Geophysical Research Letters*, **45,** 11,904-911,912, doi:10.1029/2018gl078998.

879   Yettella, V., and J. E. Kay, 2017: How will precipitation change in extratropical cyclones as the

880   planet warms? Insights from a large initial condition climate model ensemble. *Climate*

881   *Dynamics*, **49,** 1765-1781, doi:10.1007/s00382-016-3410-2.

882   Zhu, Y., and R. E. Newell, 1998: A Proposed Algorithm for Moisture Fluxes from Atmospheric

883   Rivers. *Mon. Weather Rev.*, **126**, 725–735, https://doi.org/10.1175/1520-

884   0493(1998)126<0725:APAFMF>2.0.CO;2.
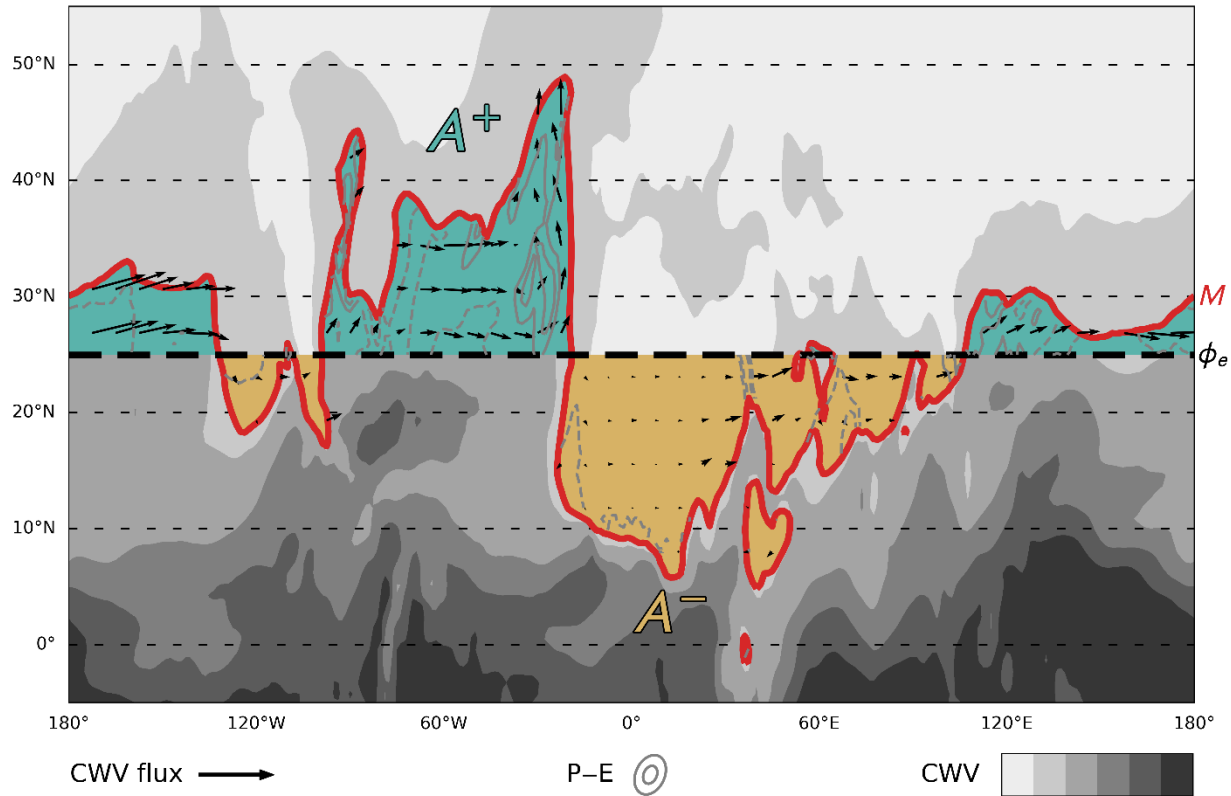
Figures

Figure 1: Schematic of the wave activity transformation. Shading represents column water vapor (in 10 kg m^{-2} increments), arrows represent the moisture transport or column water vapor flux, and grey contour lines represent the net precipitation (in 3 mm day^{-1} increments). The solid black dashed line is the equivalent latitude, chosen such that the areas in tan and those in aqua have equal areas. Integrating net precipitation from the equivalent latitude to the red contour line at a particular longitude yields the local hydrologic cycle at that longitude and (equivalent) latitude.
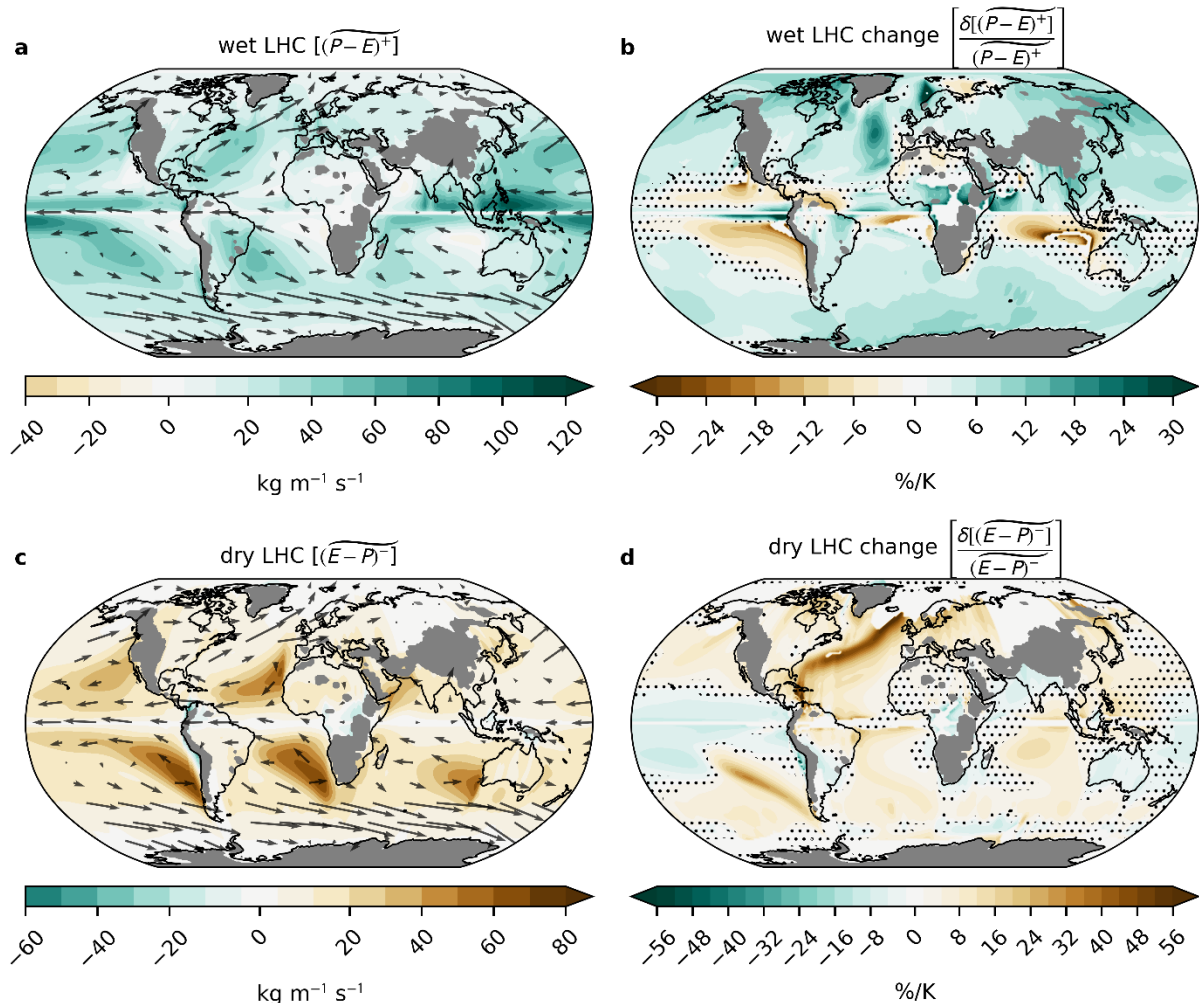
Figure 2: Annual, ensemble-mean a) present-day (1990-2005) wet local hydrologic cycle [LHC;

$(\widetilde{P-E})^+$, shading], b) RCP8.5 (2071-2080) fractional change in the wet LHC, c) present-day dry

LHC [$(\widetilde{E-P})^-$, shading], d) RCP8.5 fractional change in the dry LHC. Arrows in a) and c)

represent the annual-mean, ensemble-mean, vertically-integrated, specific-humidity-weighted

velocity (**v**), a measure of low-level tropospheric flow. All data is taken from the CESMv1 Large

Ensemble (LENS). Stippling represents regions where fewer than 85% of the 40 ensemble

members agree on the sign of the response; land surface height above 800m is masked in grey

due to the impacts of orography on computing the LHC.

47

903
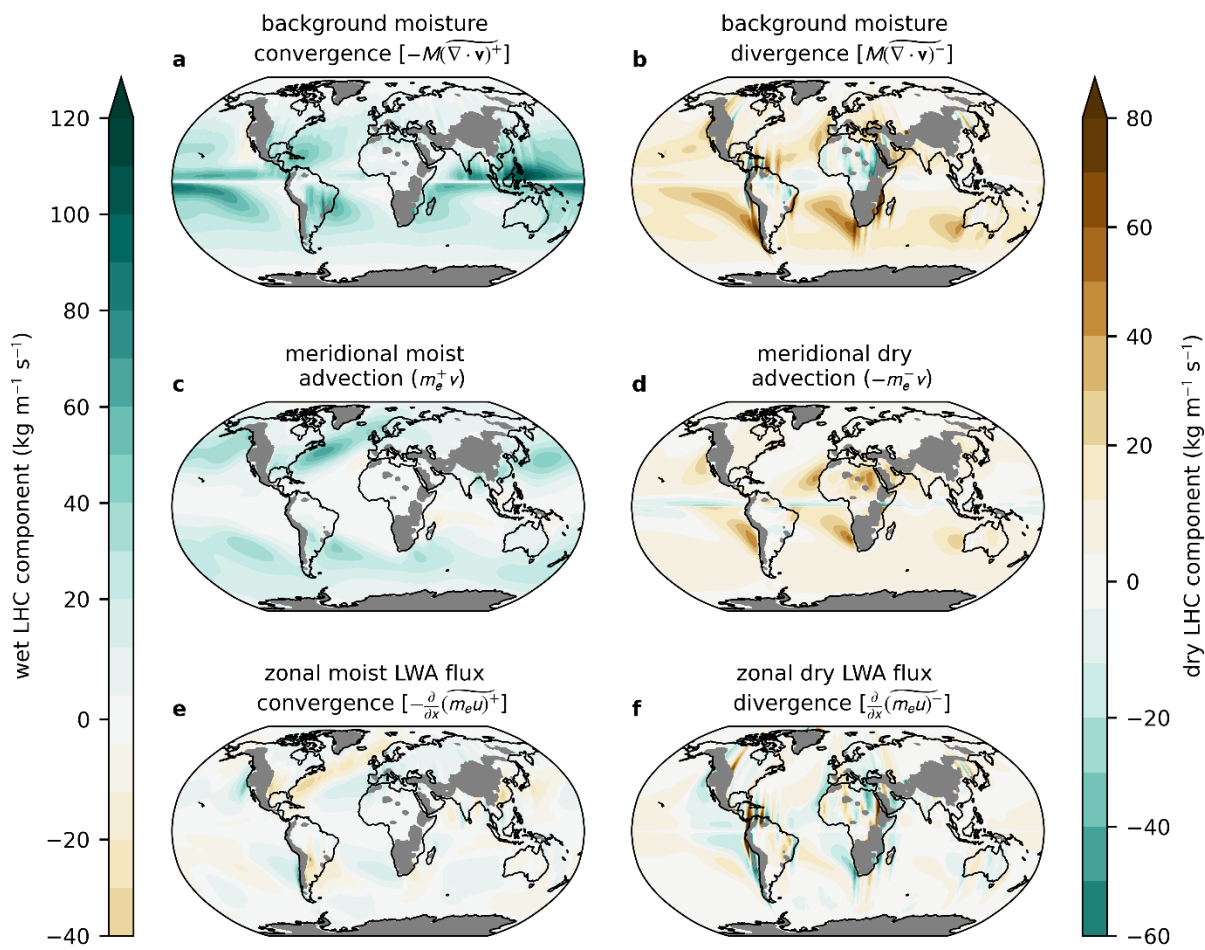
Figure 3: Annual, ensemble-mean components of the closed LHC budget for the present-day

(1990-2005) climate in CESM LENS. The LHC is balanced by the low-level (a) convergence or (b)

divergence of background moisture, meridional advection of (c) moist or dry (d) intrusions, and

the zonal (e) moist local wave activity (LWA) flux convergence or (f) dry LWA flux divergence. As

in the previous figure, land surface above 800m is masked (grey shading).

48

909
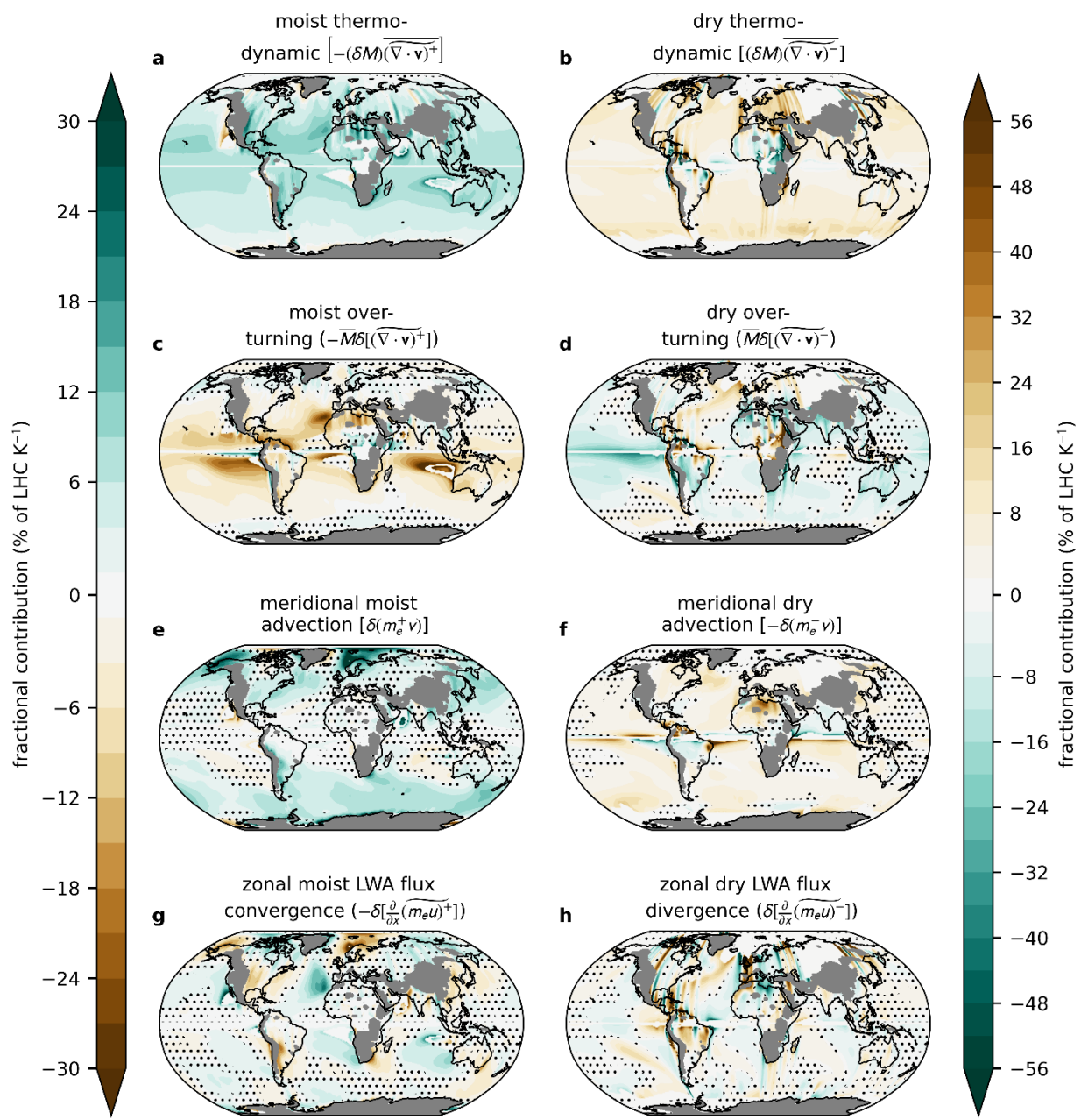
Figure 4: Fractional contributions of the different components of the LHC to the fractional

RCP8.5 change (2071-2080 minus 1990-2005) in CESM LENS. Changes in the LHC are separated

into those driven (a,b) thermodynamically, (c,d) by the overturning circulation, by the

meridional advection of (e) moist or (f) dry intrusions, and by the zonal (g) moist LWA

49

914   convergence or (h) dry LWA divergence. Contributions are determined by taking the change in

915   each budget term of Eq. (8) and dividing by the present-day wet or dry LHC so that they remain

916   additive. Stippling represents regions where fewer than 85% of the 40 ensemble members

917   agree on the sign of the response. As in previous figures, land surface above 800m is masked

918   (grey shading). Note the differing scales between wet (left) and dry (right) LHC changes, chosen

919   to align with Figures 1b and 1d, respectively.
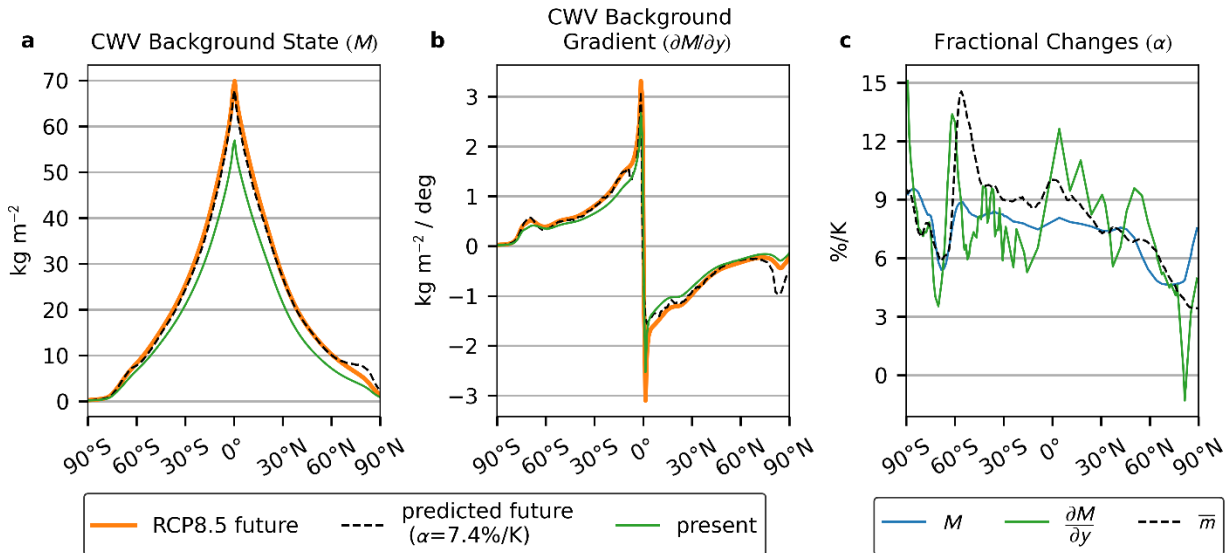
Figure 5: Using an $\alpha = 7.4\%$/K (O'Gorman and Muller 2010; Lorenz and DeWeaver 2007),

we are able to predict the future distribution of (a) the column water vapor (CWV)

background state M and its meridional gradient (b) $\partial M/\partial y$ given the present state and the

RCP8.5 change (2071-2080 minus 1990-2005) in zonal-mean temperature in CESM LENS,

utilizing (10) and (11). We also compute (c) the scaling factor α directly from RCP8.5

changes to assess where the theory holds well and to compare it to the zonal-mean CWV $\overline{m}$,

which does not follow Clausius-Clapeyron scaling as strongly as the background state M.

a moist mixing length (η^+; positive)

b dry mixing length (η^-; negative)

length scale (km)

c moist cycling rate $(\tau^+)^{-1}$

d dry cycling rate $(\tau^-)^{-1}$

HCR (days^{-1})

e participation ratio $\left(\frac{A^+ - A_c^+}{A^+} \right)$

PR

928

52
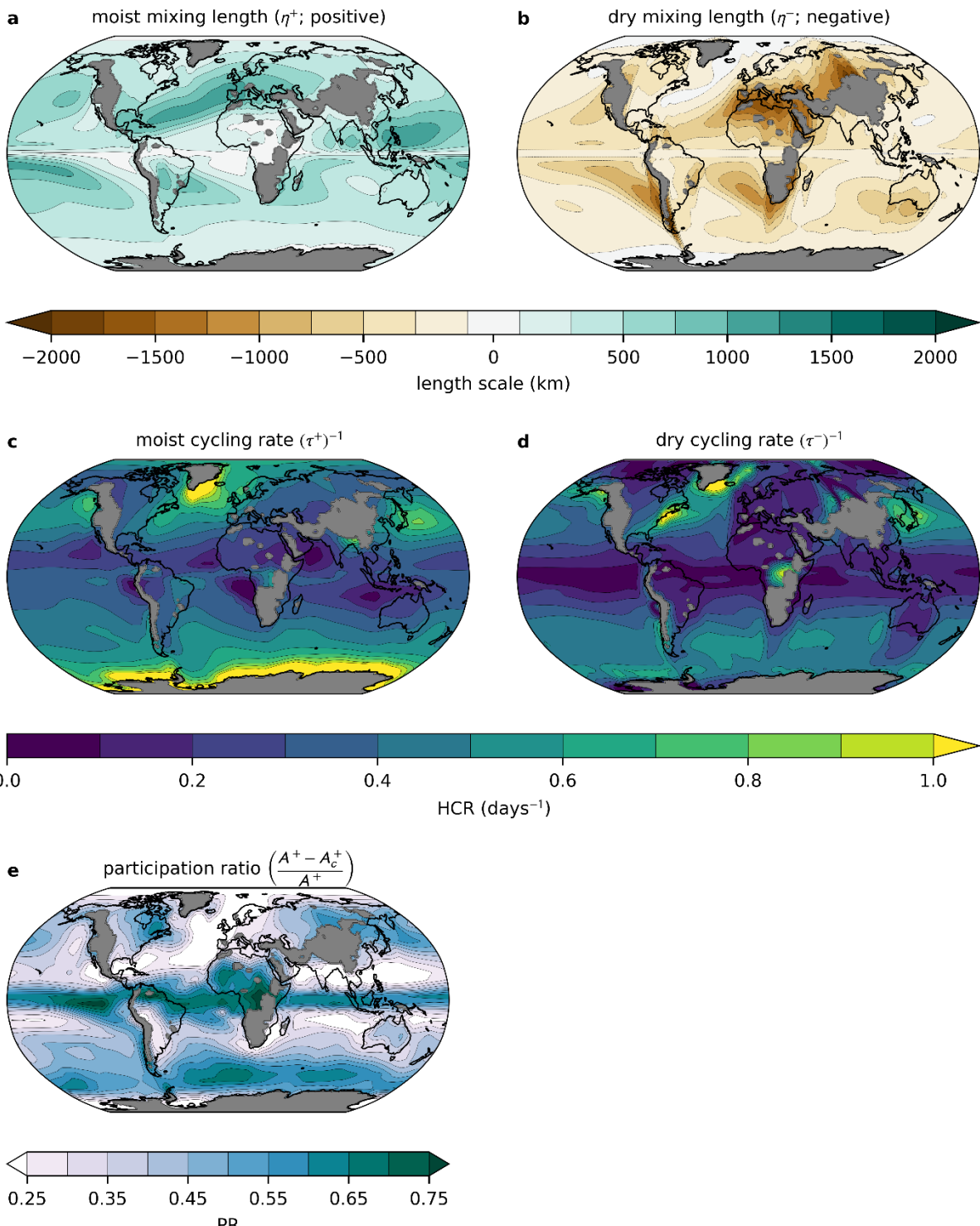
929   Figure 6: Annual, ensemble-mean mixing length scales (a,b), cycling rates (c,d), and

930   participation ratio (e) for the present-day (1990-2005) climate in CESM LENS. As in previous

931   figures, land surface above 800m is masked (grey shading).

53

932
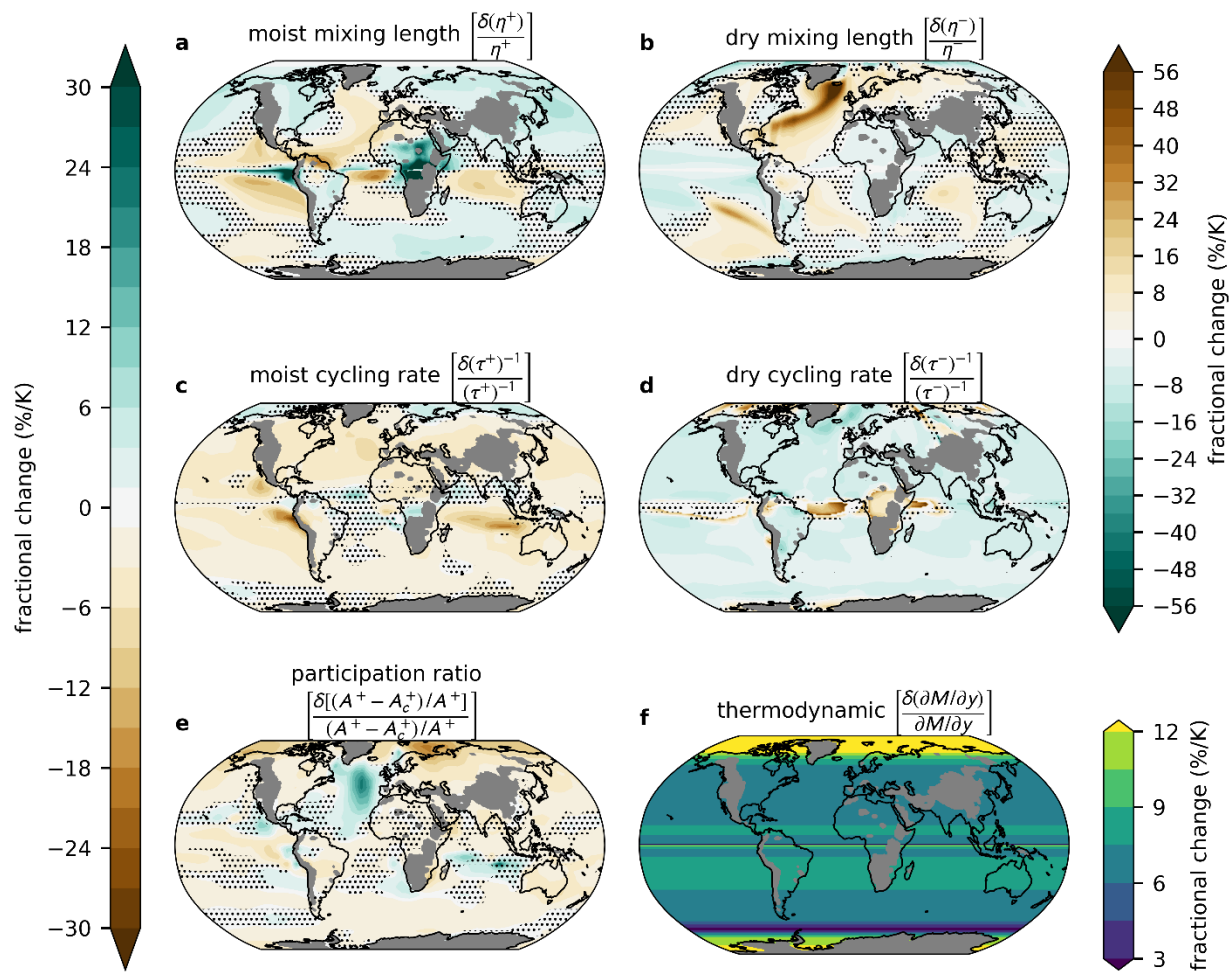
Figure 7: Annual, ensemble-mean fractional RCP8.5 (2071-2080 minus 1990-2005) changes for

(a) moist and (b) dry mixing length scale, (c) moist and (d) dry cycling rates, (e) wet LHC

participation ratio, and (f) background moisture gradient in CESM LENS. Changes in the wet LHC

consist of contributions from the background moisture gradient, moist mixing length (weighted

double the other contributions), moist timescale, and the participation ratio. The dry LHC

consists of similar contributions as the wet, except using the dry counterparts and excluding the

participation ratio. Stippling represents regions where fewer than 85% of the 40 ensemble

members agree on the sign. As in previous figures, land surface above 800m is masked (grey

shading). Note the different scales between wet and dry changes.

942
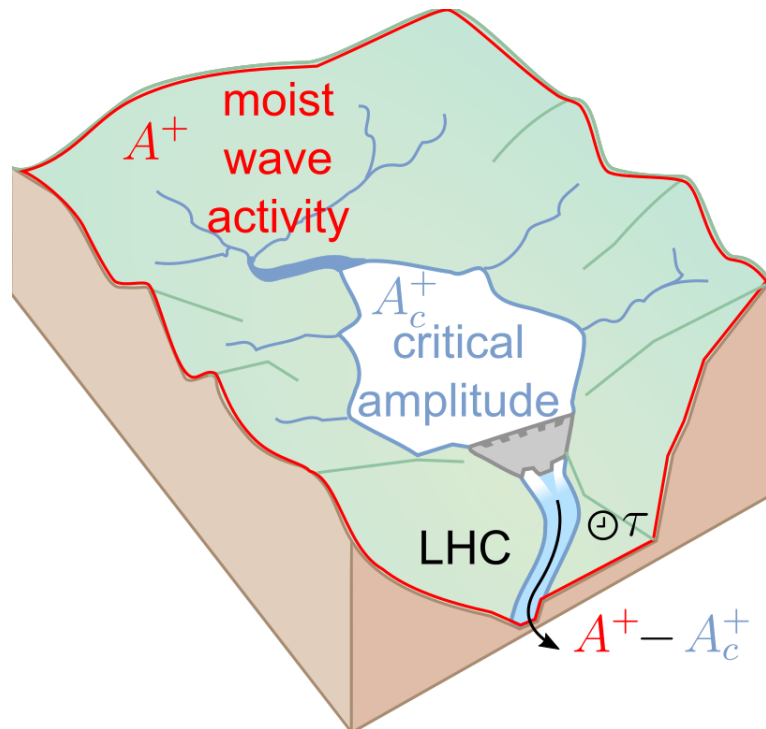
Figure 8: Schematic illustrating the different components of the LHC framework, which is akin

to a watershed with a dam or levy at its outlet.
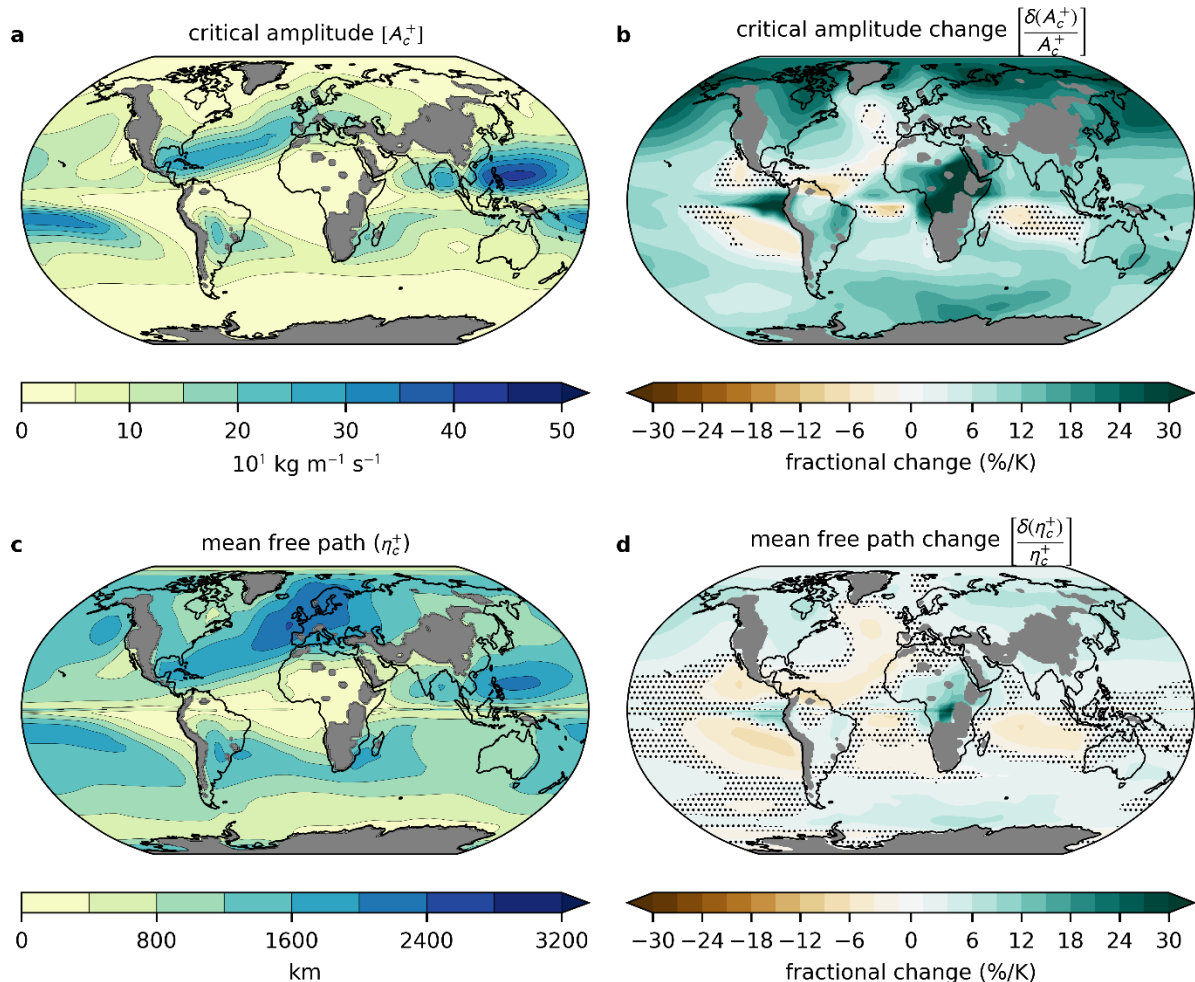
Figure 9: Annual-mean, ensemble mean a) present-day (1990-2005) reserved LHC, b) RCP8.5
(2071-2080) fractional change in the reserved LHC, c) present-day mean free path, and d)
RCP8.5 fractional change in mean free path in CESM LENS. As in previous figures, land surface
above 800m is masked (grey shading) and stippling represents regions where fewer than 85% of
the ensemble members agree on the sign.

56